JOURNAL OF GEOPHYSICAL RESEARCH: SOLID EARTH, VOL. 118, 1–21, doi:10.1002/jgrb.50130, 2013

Radiography of a normal fault system by 64,000 high-precision earthquake locations: The 2009 L'Aquila (central Italy) case study

L. Valoroso,[1] L. Chiaraluce,[1] D. Piccinini,[1] R. Di Stefano,[1] D. Schaff,[2] and F. Waldhauser[2]

Received 28 November 2012; revised 11 February 2013; accepted 12 February 2013.

[1] We studied the anatomy of the fault system where the 2009 L'Aquila earthquake (M_W 6.1) nucleated by means of ~64 k high-precision earthquake locations spanning 1 year. Data were analyzed by combining an automatic picking procedure for *P* and *S* waves, together with cross-correlation and double-difference location methods reaching a completeness magnitude for the catalogue equal to 0.7 including 425 clusters of similar earthquakes. The fault system is composed by two major faults: the high-angle L'Aquila fault and the listric Campotosto fault, both located in the first 10 km of the upper crust. We detect an extraordinary degree of detail in the anatomy of the single fault segments resembling the degree of complexity observed by field geologists on fault outcrops. We observe multiple antithetic and synthetic fault segments tens of meters long in both the hanging wall and footwall along with bends and cross fault intersections along the main fault and fault splays. The width of the L'Aquila fault zone varies along strike from 0.3 km where the fault exhibits the simplest geometry and experienced peaks in the slip distribution, up to 1.5 km at the fault tips with an increase in the geometrical complexity. These characteristics, similar to damage zone properties of natural faults, underline the key role of aftershocks in fault growth and co-seismic rupture propagation processes. Additionally, we interpret the persistent nucleation of similar events at the seismicity cutoff depth as the presence of a rheological (i.e., creeping) discontinuity explaining how normal faults detach at depth.

Citation: Valoroso, L., L. Chiaraluce, D. Piccinini, R. Di Stefano, D. Schaff, and F. Waldhauser (2013), Radiography of a normal fault system by 64,000 high-precision earthquake locations: The 2009 L'Aquila (central Italy) case study, *J. Geophys. Res. Solid Earth*, *118*, doi:10.1002/jgrb.50130.

1. Introduction

[2] To date, the literature concerning earthquake sequences occurring on normal faults is large including mainly normal faulting sequences in Italy (Norcia, 1979; Irpinia, 1980; Gubbio, 1984; Colfiorito, 1997; L'Aquila, 2009), in Greece (Kalamata, 1986; Kozani-Grevena, 1995; Athens, 1999) and in the United States (Borah Peak, 1983; Eureka Valley, 1993). The earthquake catalogues describing these sequences are usually characterized by a quite high magnitude of completeness (around $M_C \geq 2$), the minimum magnitude above which all events occurring in a study region can be reliably detected and located [*Wiemer and Wyss*, 2000]. This limitation prevents the description of the fault system architecture with a resolution greater than the kilometer scale and of the characteristics of the seismicity pattern.

[3] In the past 10 years, digital seismic archives have been growing around the world following the increasing number of three-component (3C) seismic stations deployed for both permanent and temporary monitoring of seismic activity [e.g., *Schorlemmer et al*., 2010; *Chiaraluce et al*., 2009, for the Italian region]. Moreover, a big effort has been made to furnish instruments to significantly lower the magnitude detection threshold and to improve the resolution capability of the available seismological datasets by developing automatic procedures that allow reliable detection and accurate location of large earthquake catalogues [e.g., *Rowe et al*., 2002; *Di Stefano et al*., 2006; *Waldhauser and Schaff*, 2008; *Diehl et al*., 2009; *Aldersons et al*., 2009; *Waldhauser*, 2009, and references therein].

[4] We harness these recent major improvements in seismic data acquisition, archiving, and analysis to investigate the complex fault architecture and mechanics associated with the 6 April 2009 M_W 6.1 L'Aquila earthquake, focusing on the brittle behavior of the upper crust during the foreshock and aftershock sequence. Using an accurate automatic *P* and *S* wave picking procedure [*Aldersons et al*., 2009] together with efficient cross-correlation and double-difference (DD) methods [*Waldhauser and Schaff*, 2008, and references therein], we develop the largest earthquake catalog

[1]Istituto Nazionale di Geofisica e Vulcanologia, Roma, Italy.
[2]Lamont-Doherty Earth Observatory, Columbia University, New York, USA.

Corresponding author: L. Valoroso, Istituto Nazionale di Geofisica e Vulcanologia, Roma, Italy. (luisa.valoroso@ingv.it)

2169-9313/13/10.1002/jgrb.50130

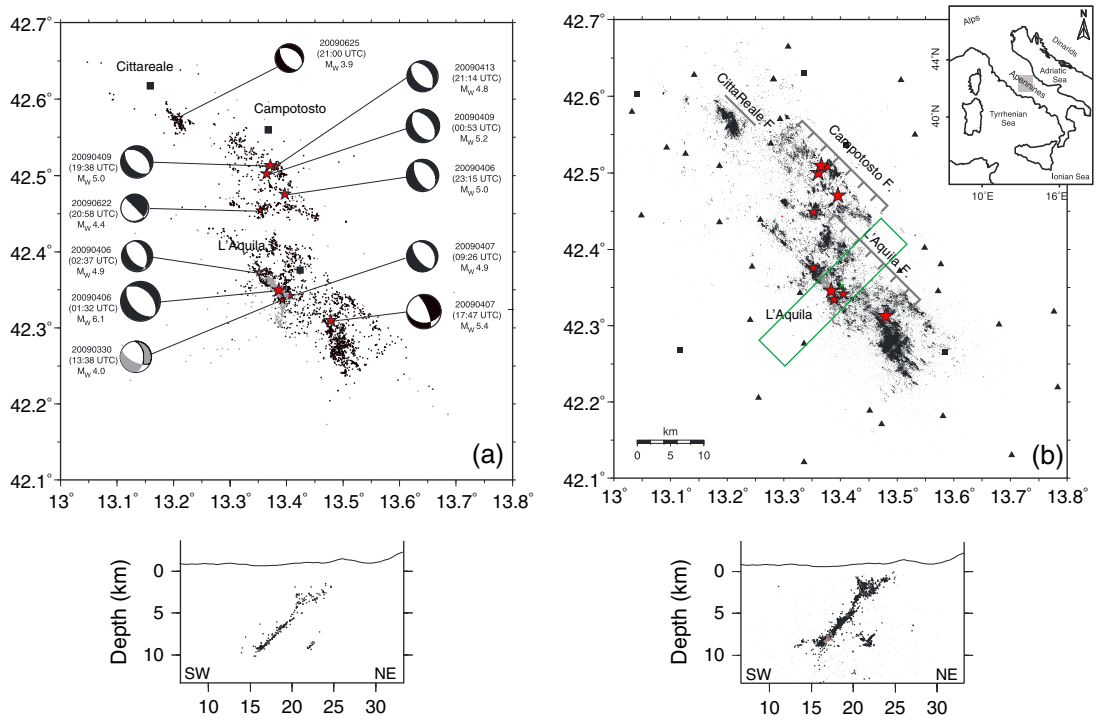

Figure 1. Map and NW-trending vertical section of the L'Aquila seismic sequence showing a comparison between a standard seismological dataset for a moderate magnitude normal faulting event made of about 3 k events (Figure 1a; redrawn after *Chiaraluce et al.* [2011a]) and the dataset presented in this study made up of 64 k events (Figure 1b). The gray dotted line in Figure 1b represents the trace of the NW-trending vertical section showing earthquakes occurring within 2 km from the vertical plane. Thick gray dots are for foreshocks, while we report in black highly correlated events (i.e., events having more than 10 *P* waves and 5 *S* waves correlated phases with at least one other event, representing 80% of the dataset) and in gray poorly correlated events (i.e., events that mostly occur off-fault in the volume around the major faults representing 20% of the dataset); focal mechanisms of the largest events of the sequence are from *Scognamiglio et al.* [2010]; red stars are events with $5.0 \leq M_W \leq 6.1$ plus the M_W 4.0 foreshock (30 March), the M_W 4.4 (22 June), and the M_W 3.9 occurred in the Cittareale area (25 June); black triangles and black squares represent temporary and permanent stations used in this study, respectively; gray lines are a schematic representation of the three main fault segments activated during the sequence, while the green box indicates the 4 km volume of seismicity projected into the vertical sections.

ever for a moderate magnitude normal faulting event. We achieved a $M_C = 0.7$ for the aftershock sequence, lowering by more than 1 unit the magnitude of completeness for the available earthquake catalogue for the sequence [*Chiaraluce et al.*, 2011a] (Figure 1a). The catalog is composed of 64,051 events covering all of 2009 (Figure 1b), with earthquake location uncertainties lower than the spatial dimension of the earthquake sources.

[5] In this paper, we build on a previous study by *Chiaraluce et al.* [2011a], who retrieved and analyzed a high-resolution double-difference catalog made up of 561 foreshocks and 2643 aftershocks with $ML \geq 1.9$ over the same time period, to study the fault geometry and the spatio-temporal seismicity evolution of the L'Aquila seismic sequence. The authors recognize two main SW-dipping normal faults, the L'Aquila and Campotosto segments, forming an en-echelon system, extending in the NW-SE direction for about 50 km (Figure 1a). The L'Aquila fault is about 16 km long showing a planar geometry with a constant dip (~48°) between 10 and 2 km depth (see vertical section to the left in Figure 1a). In contrast, the Campotosto fault, which was activated by three events with $5.0 \leq M_W \leq 5.2$, shows a listric geometry, composed of planar segments with different dips. This segment is blind with no seismic events occurring in the first 5 km of the upper crust. Smaller faults have been described such as the one located close to the Cittareale village and other secondary segments located in both the hanging wall and footwall of the major fault planes.

[6] The M_W 6.1 main shock was preceded by a foreshock sequence that lasted at least for 4 months (Figure 2, in which we show the space-time distribution of the 64,051 earthquakes through all of 2009). The foreshocks clustered at the deepest portion of the main shock fault plane within the nucleation volume along a 10 km long NW-trending segment (Figure 2). A week before the main shock on 30 March, the largest foreshock (M_W 4.0, red star in Figure 2) activated a minor antithetic off-fault segment [*Chiaraluce et al.*, 2011a]. A few hours before the main shock, the seismicity jumped back to the L'Aquila plane followed by the M_W 6.1 event main shock. A variation in the V_P/V_S ratio interpreted in terms of rock dilatancy has been reported in this time lapse, suggesting the involvement of fluids in the foreshock sequence evolution [*Lucente et al.*, 2010]. Soon after the main shock, the aftershocks activated the

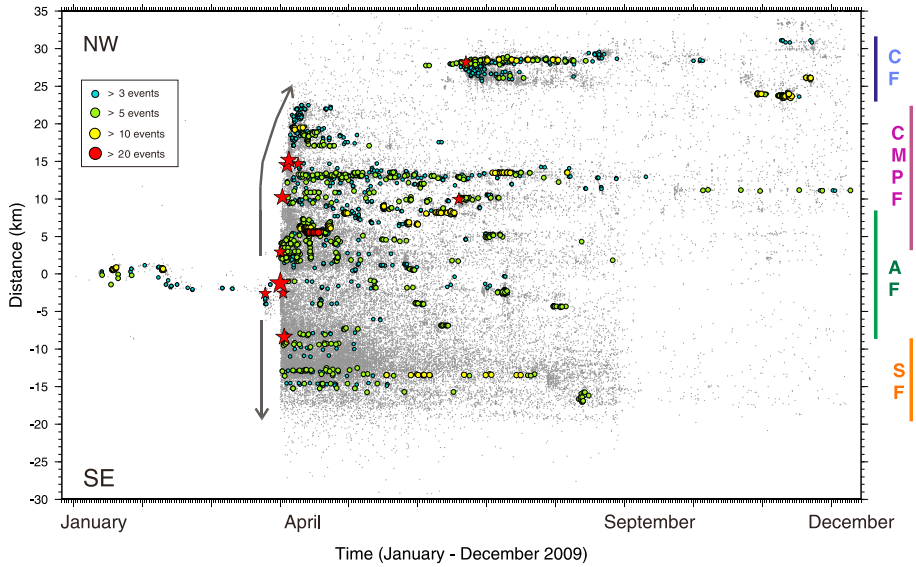

Figure 2. Spatiotemporal evolution of the seismicity in the epicentral area during the whole 2009. Red stars are events with $5.0 \leq M_W \leq 6.1$ plus the M_W 4.0 foreshock (30 March), the M_W 4.4 (22 June), and the M_W 3.9 occurred in the Cittareale area (25 June). The *y* axis represents a 65 km long N133°E trending vertical plane (intersecting the L'Aquila main shock) where we project all the events of the sequence. Gray arrows indicate the directions of seismicity migration (see text for explanation). SF: Southern Fault; AF: L'Aquila Fault; CMPF: Campotosto Fault; CF: Cittareale Fault. We also report the location of 425 co-located events clusters analyzed in this study. Events are color-coded according to the number (N) of events in each cluster.

south-easternmost sector (gray arrow pointing to the SE in Figure 2), where the unilateral rupture of the main shock was observed [*Pino and Di Luccio*, 2009]. Then the seismicity migrated toward the NW, with a migration rate on the order of 3.5 km/day (curved line pointing upward in Figure 2), where three $M_W \geq 5.0$ events activated the Campotosto fault. A pore pressure diffusion process has been invoked to model the observed seismicity migration toward the northern-eastern sector [*Di Luccio et al*., 2010; *Chiaraluce et al*., 2011a; *Malagnini et al*., 2012]. At the end of June, the seismicity activated a minor segment near the Cittareale village, following a major event with M_W 3.9 (Figures 1 and 2). By the end of 2009, the maximum length of the fault system imaged by the earthquake distribution was about 50 km in the N135°E trending direction [see *Chiaraluce*, 2012 for a comprehensive review].

[7] The sequence hit the central Apennines Mio-Pliocene fold-and-thrust belt, which was formed during the westward subduction of the Adria slab, after the consumption of the Tethys Ocean [*Malinverno and Ryan*, 1986]. The outcropping lithologies belong to the southern Tethys passive margin units: basins, ramps, and structural highs of Permo-Triassic to Miocene age [*Parotto and Praturlon*, 1975], dominated by platform, margin, and basin carbonate rocks. Since the Early Pleistocene, the central sector of the chain was affected by a NE-trending extensional tectonic regime [*D'Agostino et al*., 2001; *Montone et al*., 2004] with a current extension rate of 3–4 mm/yr [*Hunstad et al*., 2003; *D'Agostino et al*., 2008]. This extension resulted in the formation of intra-mountain basins, such as the L'Aquila basin, bounded by a complex system of NW-SE striking normal faults, in areas previously affected by compression [e.g., *Galadini and Galli*, 2000; *Patacca et al*., 2008]. Accordingly, moment tensor solutions for the largest shocks of the L'Aquila sequence [*Scognamiglio et al*., 2010; *Pondrelli et al*., 2010; *Herrmann et al*., 2011] show normal faulting kinematics (Figure 1a), consistent with the geometry of the activated fault.

[8] Here we take advantage of our new detailed foreshock and aftershock dataset, made up of 64,501 events with $Mc = 0.7$, which is 20 times larger than the dataset presented by *Chiaraluce et al*. [2011a], to furnish a more complete image of the fault system architecture. Compared to the previously imaged fault geometry, we show a large number of new small faults, and an improved description of how the seismicity is distributed along strike and depth of the major faults. Also, the dense spatiotemporal distribution of the aftershock sequence allows us to characterize the seismic decay rate within different portions of the fault system (Figure 2).

[9] Based on the importance of understanding the role of fault zone properties in controlling rupture initiation and propagation [*Boatwright and Cocco*, 1996], we will study the internal structure of the L'Aquila fault. In this way, we will contribute to the investigations of important unresolved questions about faulting and earthquake mechanics such as how the damage zones form and whether the same mechanisms govern damage zone development throughout the growth of the fault [e.g., *Cowie and Scholz*, 1992; *Rice et al*., 2005; *Mitchell and Faulkner*, 2009; *Savage and Brodsky*, 2011].

[10] We will investigate the mechanical properties of the activated faults and their spatiotemporal behavior during the preseismic and postseismic phases of the L'Aquila sequence, by focusing on the presence of clusters of similar earthquakes. Numerous sequences of similar events and/or

repeating earthquakes, i.e., events that repeatedly rupture the same fault patch with nearly identical waveforms, locations, and magnitudes [*Poupinet et al*., 1984; *Vidale et al*., 1994], have been recognized in both transform and convergent plate boundaries following large events: 1984 M6.2 Morgan Hill earthquake [*Vidale et al*., 1994; *Marone et al*., 1995; *Schaff and Beroza*, 2004; *Peng et al*., 2005], 1989 M6.9 Loma Prieta event [*Schaff and Beroza*, 2004], the 2004 M6.0 Parkfield earthquake [e.g., *Chen et al*., 2010], and for subduction zone earthquakes in Japan [e.g., *Uchida et al*., 2009]. To date, repeating earthquakes nucleating during a normal faulting seismic sequence have not been observed.

[11] We will first describe the processing used to accurately locate 4 months of foreshocks and 8 months of aftershocks of the 2009 L'Aquila sequence. Then we will analyze the spatiotemporal seismicity distribution together with focal mechanism solutions of the largest events to reconstruct the fine-scale 3-D architecture of the activated fault system and to describe the fault zone internal structure of the major faults. We will use the spatiotemporal occurrence of clusters of similar events to characterize the mechanical behavior of different portions of the fault system during the foreshock, main shock, and aftershock phases of the L'Aquila sequence. The combined analysis of these datasets will allow us to develop a seismotectonic model for the study area, by describing the behavior of active normal faults in the upper crust and their termination at the transition from seismogenic to aseismic crust.

2. Data Analysis

[12] We use seismic data recorded during all of 2009 at a very dense local network composed of 67 three-component seismic stations (Figure 1b). Twenty of these stations are permanent stations of the Italian Seismic National Network (RSNC) located within 80 km from the epicentral area (black squares in Figure 1b), while 47 temporary stations (black triangles in Figure 1b) were installed soon after the occurrence of the main shock to record the aftershock sequence [*Margheriti et al*., 2011]. The seismometers are both short period (1 s and 5 s) as well as broadband (40 s) sensors. The sampling rate is 125 Hz. In the following, we describe the data processing procedure we applied to the continuous recordings (Figure 3).

2.1. Single-Event Processing and Location

[13] Event detection from the continuous recordings was performed by applying a detection algorithm to all stations (step 1 in Figure 3). The detection algorithm process is based on the classical STA/LTA coincidence-sum algorithm applied to the trace of the 3C covariance matrix calculated over 1 s long time windows sliding with 0.5 s step on 3C waveforms filtered in the 1–15 Hz frequency band. The parameter setting is optimized to declare as many low-magnitude events as possible, resulting in a dataset made of about 500,000 declared events during all of 2009.

[14] To these events, we applied a newly developed automatic location procedure (step 2 in Figure 3) based on an automatic picking algorithm (Manneken Pix, MPX hereinafter) [*Di Stefano et al*., 2006; *Valoroso et al*., 2009; *Aldersons et al*., 2009] able to provide accurate *P* and *S* phase pickings together with an estimation of the measurement errors which allows for consistent data weighting. The excellent performance provided by the MPX automatic picking algorithm generated a homogeneously weighted and high-quality set of about 1.9 million *P* wave and 503,000 *S* wave readings. Picking uncertainty is lower than 0.024 s (three samples) for the best picked data (class 0), while phase reading errors larger than 0.4 s were discarded.

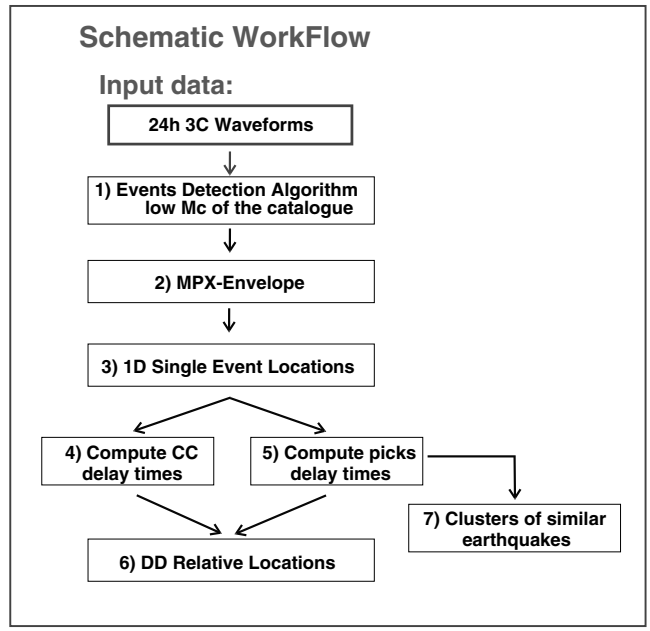

Figure 3. General overview of data flow and processing procedure followed in this study to build high-resolution relative locations catalogue for the L'Aquila foreshock and aftershock sequence.

[15] Initial locations were computed with the Hypoellipse code [*Lahr*, 1989] (step 3 in Figure 3). We used a 1-D *P* wave gradient velocity model optimized for the area [*Chiaraluce et al*., 2011b], consisting of a velocity that increases linearly from 5 km/s at the surface to 6.5 km/s at 10 km depth with a half-space below. We used a mean V_P/V_S ratios computed by using a Wadati diagram of 1.86 for the foreshock and of 1.90 for the aftershock sequence [*Chiaraluce et al*., 2011b]. After locating all detected events, we selected 133,236 events having RMS residuals less than 0.5 s, at least four *P* or *S* wave readings, azimuthal gap lower than 200°, and horizontal and vertical formal errors less than 5 km. We did not use very strict selection criteria, because the main goal in this part of the workflow was only to separate real earthquakes from falsely declared events.

[16] To exclude events that were declared 2 or 3 times by the detection algorithm, which can commonly occur during seismic sequences, we followed a three-step procedure. We first selected events with origin time in the ±3 s window. Then we chose those events having hypocentral distances less than 1 km. Finally, we used a very restrictive value of cross-correlation coefficient (i.e., ≥0.98) and delay times smaller than 0.001 (see next paragraph) to check whether those groups of events (two to four events) were the same event declared multiple times or whether they really included events closely located in space and time. This selection removed 7440 events out of the initial 133,236. The final catalog of single-event locations that is used for

subsequent double-difference processing is made of 1496 foreshocks and 124,300 aftershocks.

2.2. Cross-Correlation Measurements

[17] Cross-correlation measurements of differential traveltimes can reduce relative picking errors by an order of magnitude or more if the waveforms are similar [i.e., *Poupinet et al*., 1984; *Fréchet*, 1985; *Schaff et al*., 2004]. We used the time-domain cross-correlation function for large-scale application described in *Schaff and Waldhauser* [2005] to measure accurate differential traveltimes for correlated earthquakes (i.e., earthquakes that occur within a few kilometers of one another and have similar focal mechanisms, thus generating similar waveforms) observed at common stations. This method is able to compute differential traveltimes at subsample precision; i.e., with a sampling rate of 125 samples/s, errors in relative arrival time measurements might be less than 1–2 ms in the optimal case [*Poupinet et al*., 1984].

[18] We computed cross-correlation measurements on all event pairs with separation distances $\leq$5 km at all stations that recorded the pair (step 4 in Figure 3). Event separations were computed using 1-D initial locations. The choice of this generous inter-event distance, even if waveform similarity breaks down with increasing inter-event separation distance [i.e., *Geller and Mueller*, 1980], was intended to account for initial location errors while taking a reasonable computational time. The waveform database consists of about 27 million seismograms (vertical and horizontal components). Each seismogram was updated with *P* and *S* wave readings when available or with theoretical *P* and *S* wave traveltimes computed using the 1-D velocity model of the area. The database was then organized by calendar order and station order. Since cross-correlation measurements are performed on a station-by-station basis, we distributed the computations across 512 nodes on a Linux cluster.

[19] A large number of tests were conducted to define suitable correlation parameters that produce robust delay time measurements. Based on these tests, we ran the cross-correlation algorithm on seismograms filtered in the 1–15 Hz frequency range (the instruments are reliable in this frequency range). Correlation measurements were made for both 0.7 and 1.4 s window lengths for *P* waves and 1 and 2 s window lengths for *S* wave trains. We computed correlations at two different window lengths for each phase because this provides two separate differential time measurements that should agree for the same phase at the same station. Furthermore, we choose different window lengths for *P* and *S* wave trains because of the very complex pattern of the *P* waves and very small *S-P* times observed for many events due to small hypocenter-station distances. We search over lags of $\pm$1 s. The total processing time to compute cross correlations at all stations, once all the parameters were set, was approximately a week.

[20] We computed about 1.5 billion *P* wave and 900 million *S* wave differential times from pairs of waveforms, which had cross-correlation coefficients (CC) of 0.6 or larger. Inspection of delay time measurements with CC $<$ 0.80 suggested that a substantial amount of these measurements was outliers due to cycle skipping and correlation of noise. To avoid outliers, we also examined the consistency between the measurements obtained by using the two different window lengths at each phase [*Schaff and Waldhauser*, 2005]. Measurements with differences larger than four samples (0.032 s) were removed. For the remaining measurements, we used delay times based on the shorter window. The data selection and outlier detection procedure resulted in a high-quality database of ~190 million *P* wave and 85 million *S* wave differential time measurements with CC $\geq$ 0.85 that were used in the double-difference relocation procedure. About 70% of the dataset (87,563 events) had CC $\geq$ 0.80 with at least one other event at a minimum number of four or more stations.

[21] We compared the differences in delay times obtained by using cross-correlation measurements and picks data based on 23,432 selected events. The differences are presented in the histograms in Figure 4a, showing that 93% and 60% of the selected dataset falls within an 8 ms boundary (the sampling rate) for *P* wave and *S* waves, respectively. Eighty-three percent of the selected dataset shows differences within the sampling rate window for both *P* and *S* waves. This suggests that both cross-correlation and pick datasets identified the same phase arrival, demonstrating the good quality of the cross-correlation measurements.

2.3. Double-Difference Relocation

[22] We combined the cross-correlation differential times with 297 million *P* wave and 39 million *S* wave delay times computed from phase picks (step 5 in Figure 3) to estimate high-precision relative locations (step 6 in Figure 3) using the double-difference (DD hereinafter) algorithm *hypoDD* [*Waldhauser and Ellsworth*, 2000; *Waldhauser and Schaff*, 2008]. The DD method is an iterative least squares procedure that relates the residual between the observed and predicted phase traveltime difference for pairs of earthquakes observed at common stations to changes in the vector connecting their hypocenters through the partial derivatives of the traveltimes for each event with respect to the unknown [*Waldhauser and Ellsworth*, 2000]. The robust DD method minimizes the effects of unknown Earth structure, without the need for station corrections, by incorporating ordinary absolute traveltime measurements and/or cross-correlation *P* and *S* wave differential traveltime measurements. Residuals between observed and theoretical traveltime differences (or double differences) are minimized for pairs of earthquakes at each station while linking together all observed event-station pairs. A least-squares solution is found by iteratively adjusting the vector difference between hypocentral pairs.

[23] For the 125,796 events in the single-event 1-D catalog, which includes both foreshocks and aftershocks, we computed differential traveltimes from each event to its 40 nearest neighbors within 10 km distance (step 5 in Figure 3). Only 40 of the highest quality differential times per event pair are selected. Also, only event pairs with at least eight phases observed at common stations were used to ensure robustness of the double-difference inversion. The final selection includes 97,877 events. Both pick and cross-correlation differential times are combined in a dynamically weighted DD inversion. We parallelize the relocation process by generating 84 rectangular boxes centered on the general SW-NE strike of the main faults, each box including events connected through a web of differential time links not exceeding 3 million. Each box overlaps with its neighboring box by 70% of the surface. We require a continuous chain of pair connected events with a link strength of 11

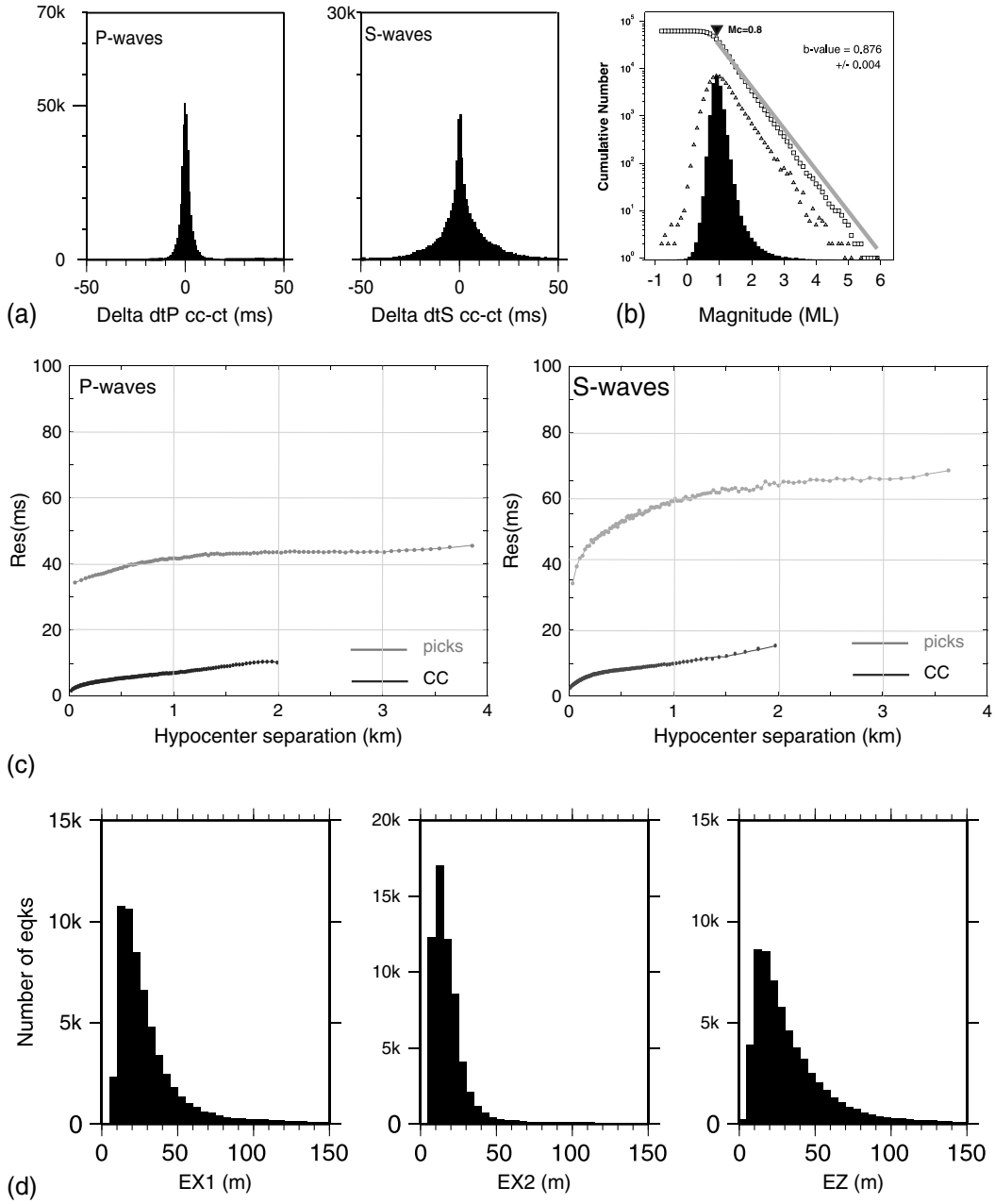

Figure 4. (a) histograms of the differences between *P* and *S* wave delay times computed by using cross-correlation measurements and picks data; (b) histogram showing the frequency-magnitude distribution for the whole catalog; the completeness magnitude (MC) and the b-value have been computed using the ZMAP code [*Wiemer*, 2001]; (c) *P* and *S* waves median final location residuals for picks and cross-correlation data shown as a function of hypocenter separation distance, within bins including 30,000 observations; (d) histograms of horizontal and vertical relative location errors, computed from the mayor/minor axes (EX1, EX2) of the horizontal and vertical (EZ) projection of the 95% confidence ellipsoids obtained from a bootstrap analysis of the final double-difference vector based on 200 samples with replacement.

differential times from stations within 100 km from an event pair's centroid. Each box undergoes a series of 25 iterations, during which the weighting of the delay time data is dynamically adjusted as a function of event separation and delay time residuals. 1-D locations are used as starting locations, and the locations and partial derivatives are updated during each iteration. We use the same local 1-D layered velocity model, which we used to compute the starting locations, to locally predict traveltimes and partial derivatives. During the first 15 iterations, the algorithm was only run by using the full weight on phase picks while the cross-correlation data were down-weighted by a factor of 100, to remove the influence of velocity model error over long distance ranges and to avoid potential station bias associated with the cross-correlation measurements [*Waldhauser*, 2001]. As the locations improve and inter-event distances become more accurate, the data derived from waveform correlations were increasingly weighted relative to the pick data (100:1)

during iterations 16–25 because of their higher measurement accuracy over shorter distance ranges. In this way, the location precision of correlated events is controlled by the accuracy of the cross-correlation data, while those events that do not correlate is controlled by the accuracy of the pick data [*Waldhauser*, 2001]. Equal weights are kept for *P* wave and *S* wave for both pick and cross-correlation data. Proper damping of the LSQR [*Paige and Saunders*, 1982] solutions is determined by investigating the condition number of the system of linear equations and the rate of convergence. HypoDD output parameters (e.g., RMS, data outliers, and convergence rate) summarizing robustness of the DD solutions in each of the 84 relocation boxes were subsequently screened, and boxes with suspicious output values (about 1% mostly because of numerical instabilities during inversion) inspected and reprocessed manually. DD solutions from each box were combined into a single catalog composed by a weighted location average of each event included in more than one box, with the weight being a linear function of an event's distance from the centroid of the cluster it belongs to [see *Waldhauser and Schaff*, 2008 for details].

[24] The final DD catalogue includes 64,051 events occurring between 1 January and 31 December 2009 (Figures 1b and 2). About 35% of the initial 97,877 events were recorded at less than eight stations, our threshold for double-difference processing, and were therefore not relocated. The relationship between the magnitude and the total number of events of the final catalogue is reported in Figure 4b, showing an averaged Mc of 0.88, while we find a Mc of 0.7 when we consider only the catalog of aftershocks from 16 April (10 days after the main shock) to the end of 2009. The M_C and the b-value have been computed using the ZMAP code [*Wiemer*, 2001]. The root mean square (RMS) residuals of the weighted pick and cross-correlation differential time for the relocated events is 0.075 s, compared to 0.122 s before relocation.

[25] In Figure 4c, we show *P* and *S* wave final location residuals for picks and cross-correlation data as a function of the hypocentral separation distance. Each statistic is computed for bins of 30,000 observations. At near-zero separation distances, the residuals reflect only measurement errors for the two data types [*Schaff et al*., 2004]. Most of the *P* and *S* wave cross-correlation residuals are less than 8 ms, which is the sampling interval. Pick residuals are larger. Relative location errors are estimated for each event by bootstrapping with replacement, the final unweighted double-difference residual vector [*Waldhauser and Ellsworth*, 2000]. Error ellipsoids are obtained at the 95% confidence level for 200 bootstrap samples. The distribution of the horizontal major/minor axis and of the vertical projections of these ellipsoids is shown in Figure 4d. The median values of the distribution along the major horizontal, minor horizontal, and vertical directions are 0.024, 0.015, and 0.027 km, respectively, while the mean values are 0.178, 0.039, and 0.087 km.

3. Fault System Architecture and Kinematics

[26] We use the spatial distribution of the 64,051 earthquakes to unravel the fault system architecture and to investigate the faulting pattern associated with the network of major and minor faults. We construct a set of 35 vertical sections oriented N45°E, perpendicular to the mean strike of the major faults. Black, gray, and white lines in Figure 5 correspond to the vertical sections shown in Figure 6 and reporting earthquakes occurring within 2 km (±1 km), 1 km, and 0.5 km from the vertical plane. We used different widths for the vertical sections in order to better image the geometrical complexity that the fault system shows along strike. Foreshocks and aftershocks are shown with red and black dots, respectively. In each vertical section, we report the location of the mapped co-seismic surface ruptures reported by *Boncio et al*. [2010] along the Monte Stabiata (MSF) and Paganica-San Demetrio (PaF-SDF) fault (gray thick lines in Figure 6 and yellow thick lines in the map in Figure 5), as well as the mapped normal faults of the area (green lines in Figure 5] [*Emergeo Working Group*, 2009; *Boncio et al*., 2010; *Galli et al*., 2010]. Also, we show the regional moment tensor solutions computed by *Herrmann et al*. [2011] for 116 events with $M_W \geq 2.7$ (red and gray beach balls represent large and moderate magnitude events, respectively).

[27] We will first describe the seismicity pattern of the major L'Aquila and Campotosto segments with the associated complex network of smaller secondary faults and then the geometry of the fault system termination to the SE and NW.

3.1. The L'Aquila Fault

[28] The geometry of the L'Aquila fault (AF) is imaged by the spatial distribution of the aftershocks that followed the M_W 6.1 main shock, which nucleated at 8.27 km depth (red star in section 9 in Figure 6b). Our main shock location is slightly shallower compared with the one computed by *Chiarabba et al*. [2009] equal to 9.46 km and *Chiaraluce et al*. [2011a] equal to 8.64 km. The AF breaks the entire upper crust from ~10 km depth to the surface, dipping 50° (±2°) to the SW, while its length is about 18 km along the N137°E direction (sections 5–13 in Figures 6 and 5). The fault architecture is complicated by a complex pattern of small (tens to hundreds of meters) secondary faults associated with the AF.

[29] Traversing along strike from SE to NW (sections 5–13 in Figure 6b), we first image the AF in sections 5a and 5b, where the aftershocks are aligned along a thin plane, a few tens of meters wide, between 10 and 3 km of depth. We emphasize that in this paragraph, we define the width of the fault zone based on the distribution of the aftershocks in the vertical sections. Moving northward (sections 6), the fault plane is not continuous but earthquakes occur on small SW-dipping fault segments about 1 to 2 km long and tens of meters thick, with coherent normal faulting focal mechanisms. Minor antithetic secondary segments intersect the main fault plane. In sections 7 and 8, the AF is again continuously imaged between 10 and 3 km of depth. The fault zone is about 300 m thick in sections 7a and 7b, showing a slight change in dip near the intersection with a minor NE-dipping fault (section 7b). In sections 8a and 8b, the aftershocks are more diffuse and define a thicker (~ 500 m) zone. In both sections 7 and 8, minor synthetic and antithetic secondary structures, tens of meters long, occur both in the AF hanging wall and footwall. In proximity to the main shock hypocenter (sections 9a and 9b), the AF is imaged between 10 and 3 km of depth. The distribution of the aftershocks along the dip of the rupture plane is irregular: the deep portion of the fault zone where the main shock

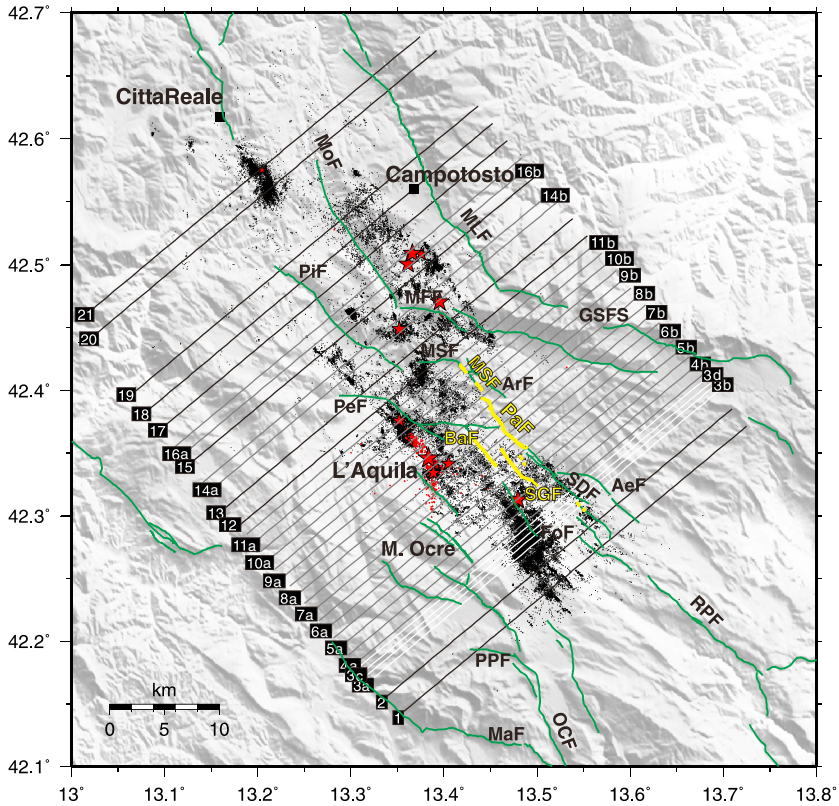

Figure 5. Map view of the relocated foreshocks (red dots) and aftershocks (black dots) with traces of the active mapped faults (green lines) and co-seismic surface ruptures (yellow lines) [after *Boncio et al.*, 2010]. Stars represent the location of the largest events of the sequence. Black, gray, and white lines correspond to the vertical sections reported in Figure 6 and showing earthquakes occurring within 2 km, 1 km, and 0.5 km from the vertical plane. The acronyms of the active faults are the following: MoF, Montereale fault; MLF, Mt. della Laga fault; PiF, Pizzoli fault; MFF, Mt. San Franco fault; MSF, Monte Stabiata fault; GSFS, Gran Sasso fault system; PeF, Pettino fault; AsF, Assergi fault; BaF, Bazzano fault; PaF, Paganica fault; SDF, San Demetrio fault; AeF, Aterno fault; SGF, San Gregorio fault; FoF, Fossa fault; RPF, Roccapreturo fault; PPF, Piani di Pezza fault; OCF, Ovindoli Celano fault; MaF, Magnola fault.

nucleation started is about 200 m thick (section 9a), while the fault zone thickens upward between 7 and 4 km of depth (section 9b). The retrieved fault image resembles the complex geometry of a dilational jog observed by field geologists on outcrops of normal faults developed in carbonate rocks [e.g., *Collettini et al.*, 2003; *Agosta and Aydin*, 2006; *De Paola et al.*, 2008]. Very few earthquakes occur at depths <4 km. This absence of seismicity in the shallow portion of the fault corresponds well with the location of a patch of co-seismic slip propagating up-dip from the main shock we will describe later. Northward (sections 10), multiple antithetic and synthetic fault splays, tens of meters thick, branch off the main fault plane to reach the surface, resembling a flower structure.

[30] Most of the focal mechanism solutions of events nucleating on the AF have pure dip-slip kinematics with one of the two nodal planes dipping at high-angle to SW, thus consistent with the aftershock alignment. Minor variations occur for smaller events at shallow depth (sections 8 in Figure 6). Moreover, focal mechanisms of events nucleating at the base of the activated fault plane show a rotation towards lower dip angles (sections 10b and 11a in Figure 6). We will further investigate this aspect in the following sections.

[31] We find a geometrical correspondence between the co-seismic ruptures mapped at the surface along the Monte Stabiata (MSF) and the Paganica-San Demetrio (PaF-SDF) geological faults (yellow traces in Figure 5 and gray thick lines in vertical sections in Figure 6) and the surface projection of the seismically imaged AF. The match is unambiguous in sections 10 and 11, where aftershocks close to the surface correlate with the surface trace of the MSF. On the contrary, the lack of seismicity near the surface in sections from 5 to 9 prevents us from evaluating the exact correspondence between the fault imaged at depth by the seismicity distribution and the mapped PaF-SDF segment. Surface ruptures were also observed along the NE dipping Bazzano (BaF) and the SW-dipping San Gregorio (SGF) faults (yellow lines in Figure 5), which are located in the AF hanging wall (sections 5–8), but no earthquakes have been located on the projection at depth of these structures.

[32] The AF termination at the two fault tips along strike shows differences both in terms of geometry and seismicity pattern. To the SE, where the largest rupture directivity has been modeled [*Pino and Di Luccio*, 2009], the AF terminates about 12 km south of the main shock (sections 1–5), in correspondence with an abrupt increase in geometrical complexity. The seismicity does not image a single fault plane, but it is distributed among a dense network of minor (tens of meters thick and 3–4 km long) sub-parallel

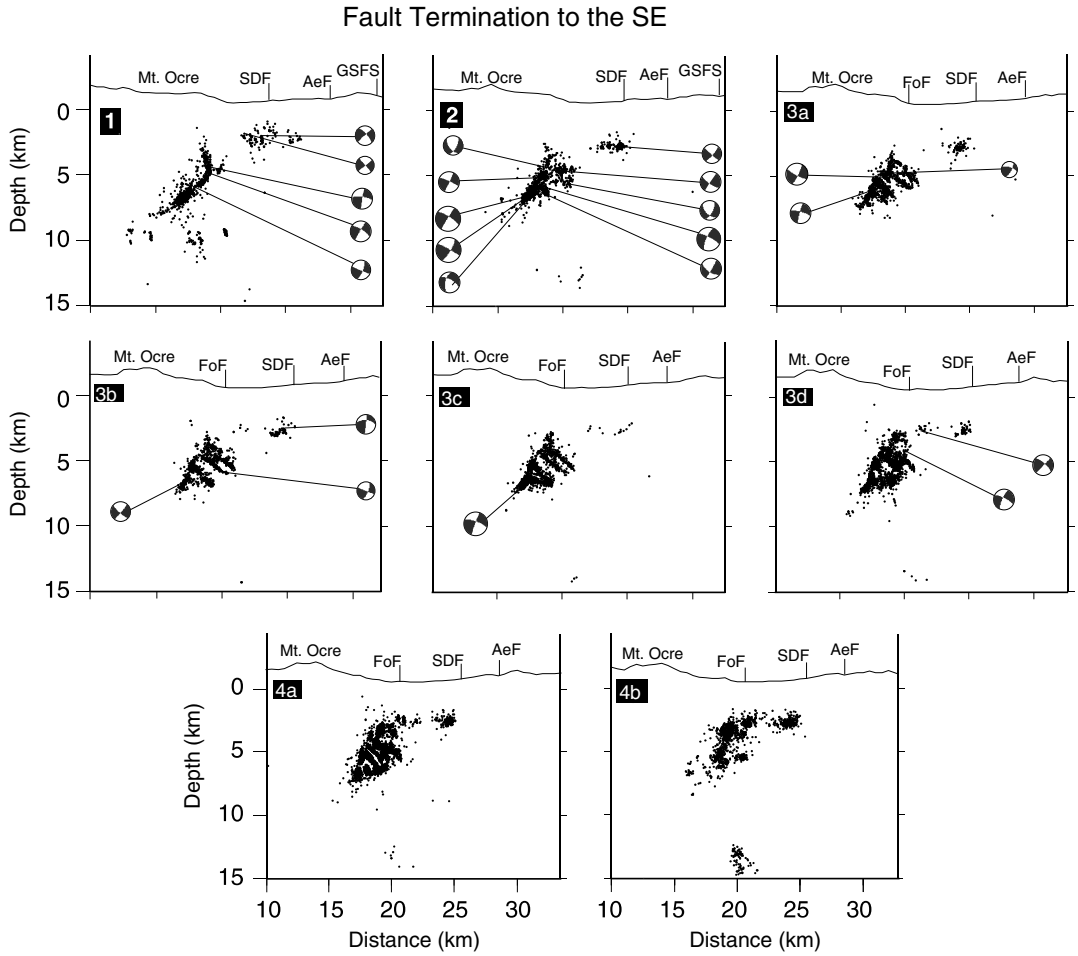

Figure 6. Set of 33 vertical sections showing the foreshocks (red dots) and aftershocks (black dots) distribution at depth. The location of the intersections between the active faults reported in Figure 5, and the sections is also reported. The acronyms are the same reported for Figure 5. We also show focal mechanisms of the largest events (red and gray beach balls are for events with $M_W \geq 4.4$ and events with $2.7 \leq M_W \leq 4.4$, respectively). (a) Details of the southern termination of the fault system; (b) the L'Aquila fault segment; (c) the Campotosto fault segment.

structures (sections 3a–3c in Figure 6a). In detail, at shallow depth in sections 5 and 6a, events image a set of small sub-parallel NE-dipping faults, with consistently oriented high-angle focal mechanisms, sandwiched between two major shallow SW-dipping structures with the resulting geometry resembling bookshelf faulting (section 5). Further south (sections 4a and 4b in Figure 6a), the deformation is more diffuse and does not cluster on clear minor structures. In sections 2 and 3a–3d, another change in fault geometry is observed with events occurring along a set of sub-parallel structures located in the footwall of a SW-dipping structure. We underline that this portion of the fault system, where the rupture directivity was observed [*Pino and Di Luccio*, 2009], shows a low seismic decay rate, characterized by the production of a large number of low-magnitude events (southern fault, SF in Figure 2). In this southern sector of the fault system (sections 4b–5b), a sequence of deep aftershocks (14–16 km), with the largest occurring on 17 April at about 14 km depth with a M_W 5.4 (sections 4 and 5 in Figure 6), activated a high-angle, NE-dipping, normal fault antithetic to the AF, as expressed by both seismicity structure and focal mechanism. Interestingly, this event coincides with the major change in the geometry of the AF termination to the SE (sections 4b–5b in Figure 6).

[33] To the NW, the AF termination zone is unambiguously imaged up to section 13, but we underline that seismic events also occur along a contiguous fault, with events nucleating in the 9 to 5 km depth range (sections 13–15 in Figure 6c). We cannot directly associate these events to the mapped active faults of this sector of the fault system, i.e., either the Pettino fault (PeF) or the Monte San Franco fault (MFF), or the Montereale Fault (MoF) because of the lack of seismicity at shallow depth. However, we emphasize that the AF might show a lateral connection with contiguous active normal faults. This has been also suggested by recent paleoseismological investigations [*Galli et al.*, 2011].

[34] In the transition zone between the two major faults, the AF and Campotosto Fault (CMPF) segments (sections 10–13), numerous sub-parallel minor structures located between 7 to 9 km depth range, accommodate part of the deformation both in the hanging wall and footwall of the AF. These zones of aftershock activity are about 500 m thick and 3 km long. Furthermore, a complex extensively developed network of smaller secondary faults occurs in the

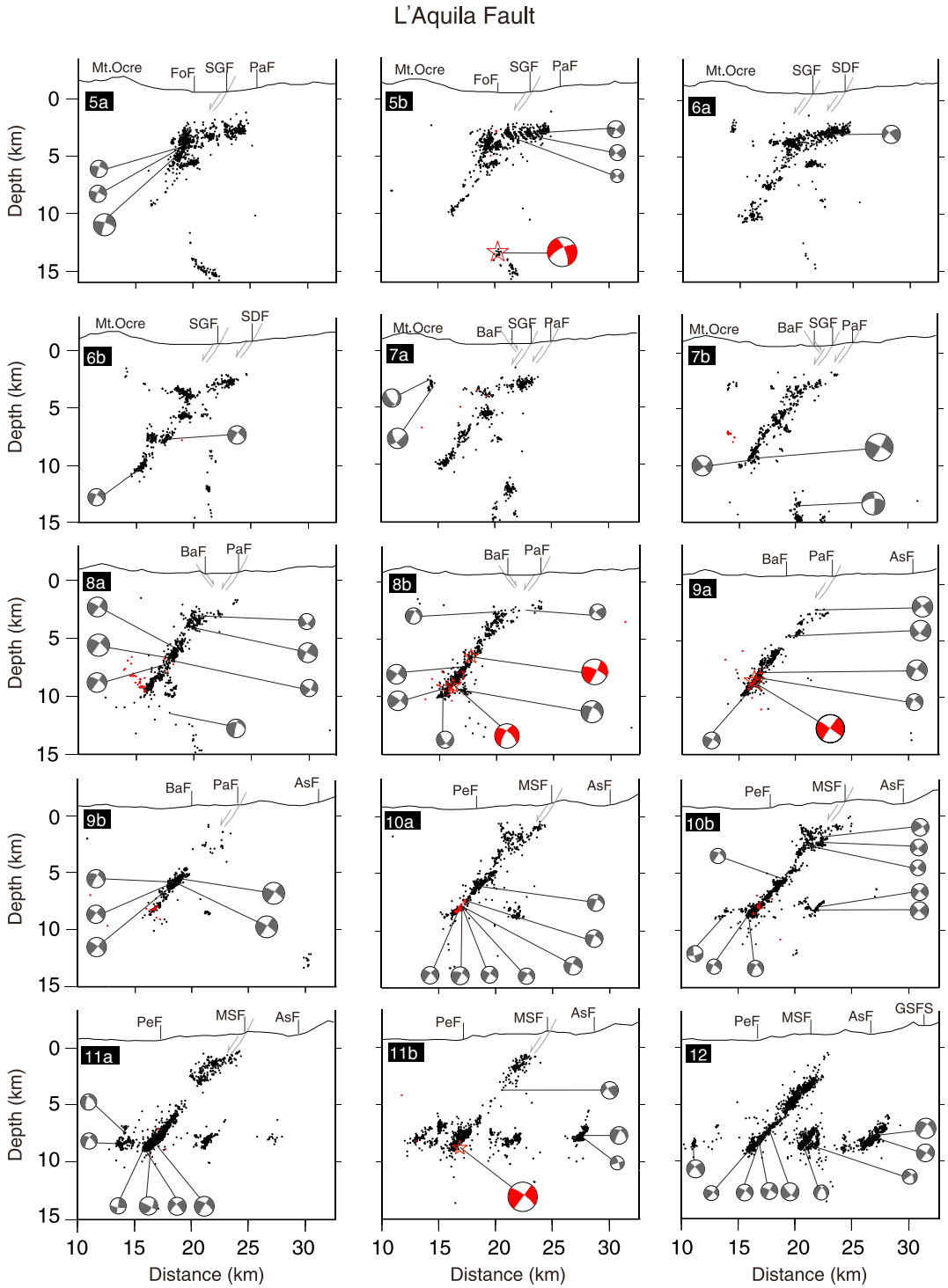

Figure 6. (Continued)

AF hanging wall (sections 11a and 11b in Figure 6b). Because of the absence of events shallower than 7 km depth, a direct comparison between these structures and the traces of mapped surface ruptures is difficult. The abrupt seismicity cutoff at 9 km depth defines a laterally continuous structural element of this portion of the fault system. The spatiotemporal seismicity pattern of this portion of the fault system is characterized by a high and long-lasting seismicity production (see the transition zone between the AF and the CMPF in Figure 2).

3.2. The Campotosto Fault

[35] The Campotosto fault lies NW of the AF fault, forming a right step with the AF (Figure 1). Along strike, it is continuously defined by the aftershocks distribution for a strike length of ~16 km (Figure 5 and sections 11–19 in Figure 6). Along dip, the aftershocks are confined from 5 to 11 km depth, with a complete lack of aftershocks at shallow depth resulting in a blind fault (sections 13–18 in Figure 6c). The CMPF is not a plane but shows a decreasing dip angle with depth from about

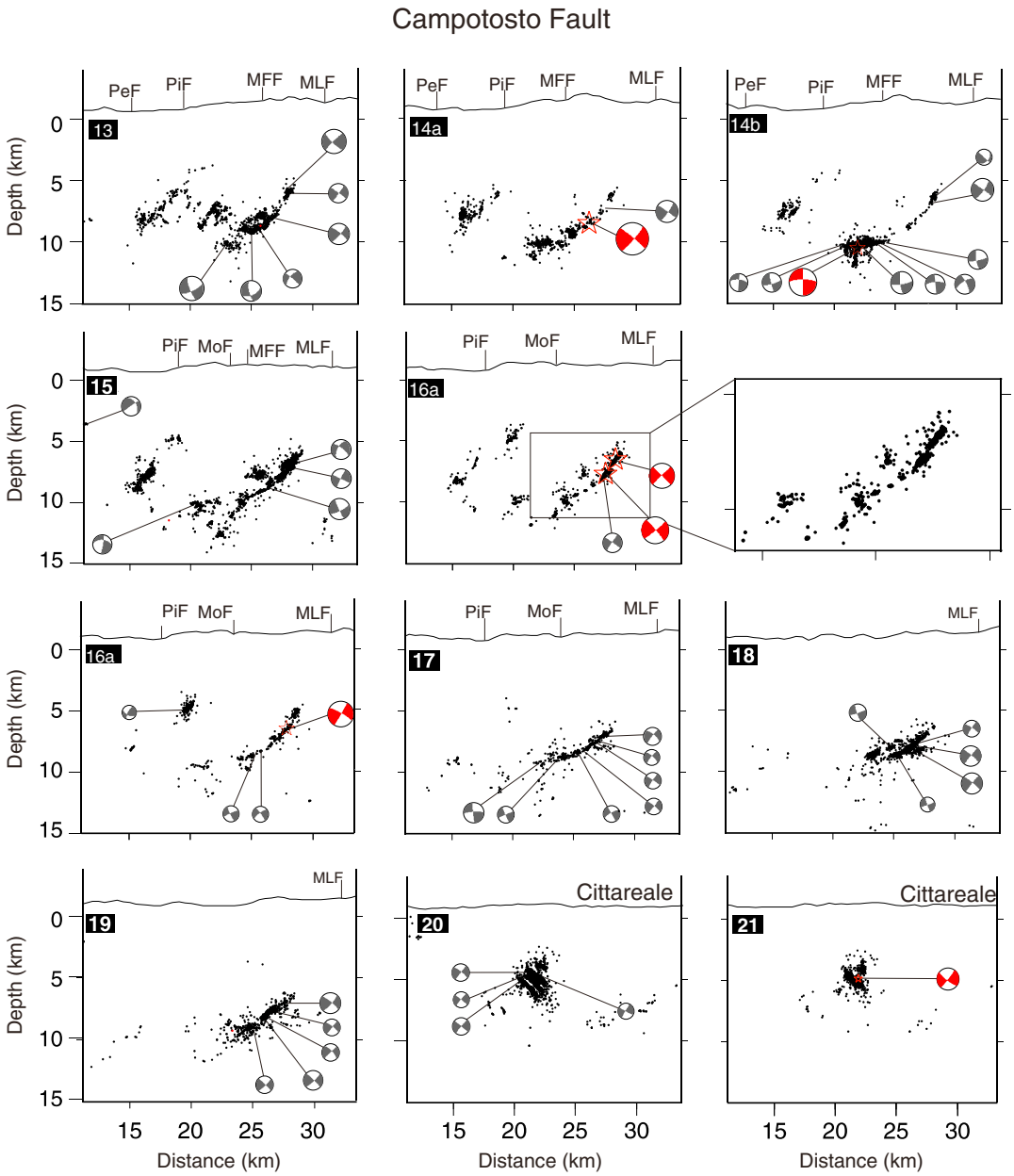

Figure 6. (Continued)

45–50° to SW (between 5 and 8 km of depth) to a nearly horizontal plane (<20°) at ~11 km depth (sections 13–16). The overall picture shows a clear listric geometry. Focal mechanism solutions of the largest events perfectly agree with this fault geometry (sections 14–16). We observe (i) an almost continuous decrease of the dip angle with depth in those sections where no large events occur (sections 13, 15, and 17) and (ii) the fault surface defines a piecewise (kinked) geometry showing major dip changes in correspondence with large events (see sections 14 and 16 and the inset in Figure 6C). In particular, in section 16a, it is possible to clearly recognize the two fault segments activated by the M_W 5.0 and M_W 5.2 events with related aftershocks.

[36] Secondary structures are imaged in the CMPF hanging wall such as the small 2 km long and tens of meters thick fault shown in section 13. A similar structure is also observed further north, intersecting the CMPF where there is a major change of the dip angle at about 7.5 km depth (section 15). In the CMPF footwall, some events nucleate on a very thin (tens of meters) structure branching off the main fault and activating a deeper portion of the crust down to 15 km of depth (section 15). Furthermore, small subvertical structures are observed right below the flat portion of the CMPF (section 14b). Interestingly, the largest among these vertical faults occurs very close to the hypocenter location of a M_W 4.4 event, whose focal mechanism shows one of the two nodal planes dipping at very low angle to the SW (dip < 10°; red focal mechanism in the lower part of section 14b). This makes it difficult to determine the activated fault plane. However, we prefer the hypothesis that the large event nucleated on the vertical plane that is imaged by subsequent aftershocks.

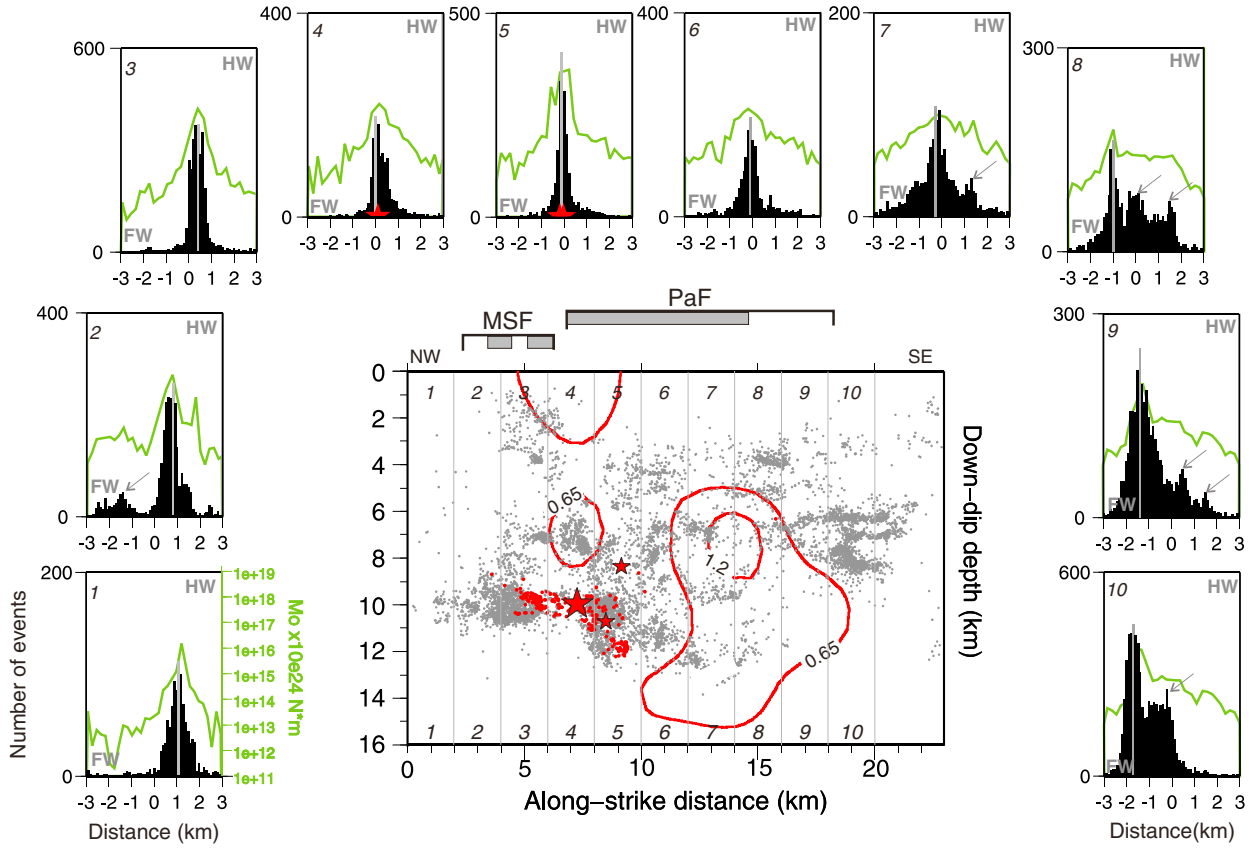

Figure 7. Down-dip fault section (strike N133°E and dip 50° to the SW) of the L'Aquila fault plane containing foreshocks and aftershocks occurring ±500 m from the fault plane (red and gray dots, respectively); $M_W \geq 4.4$ events (red stars); the co-seismic slip (red solid contours) computed by *Cirella et al.* [2012] by inverting strong motion, GPS, and DInSAR data; and Mt. Stabiata (MSF) and Paganica (PaF) mapped faults (thick black lines) and surface ruptures (thick gray lines) [*Boncio et al.*, 2010]. Rectangular boxes numbered from 1 to 10 indicate the 2 km long volumes in which the fault plane has been divided to investigate variations of the fault zone width along strike (from NW to SE). The histograms show the number of events occurring, every 100 m, within 3 km from the ideal fault plane in each box, in the fault hanging wall (HW) and footwall (FW); the events with $M_W \geq 4.4$ occurring on the fault plane (red stars); the peak of the distribution (gray bars); and the cumulative seismic moment M_0 (green lines); gray arrows point to off-fault secondary structures.

[37] The CMPF termination along strike shows lower geometrical complexity than the AF. To the SE, events occur between 10 and 7 km depth on a small (i.e., about 2 km long and tens of meters thick) zone of seismicity located in the AF footwall (sections 11 and 12 in Figure 6b). At the northern termination, events occur on a very thin seismicity zone dipping at low angle (<20°) to SW (sections 17–19). Minor antithetic and synthetic structures intersect this fault (section 18).

[38] The mapped active fault in this sector of the fault system is the Monti della Laga fault (MLF in Figures 6 and 7). The relationship between the mapped MLF and the seismological CMPF fault is not straightforward due to the lack of seismicity in the first 5 km of depth. Furthermore, a projection of the steepening trend to the surface is necessary to connect the CMP seismic fault with the surface trace.

[39] The cluster of seismicity activated near the Cittareale village, which we have called the Cittareale fault (CF in Figure 2), occurs on a set of sub-parallel small faults, 2 to 3 km long and about 100 m thick (sections 20 and 21 in Figure 6). This peculiar faulting pattern is similar to that observed at the southernmost termination of the L'Aquila fault (sections 3a–3d in Figure 6a). Also the temporal evolution of the seismicity is similar, with a sustained seismic release of low-magnitude events (see the CF and SF in Figure 2). The volume defined by the microseismic activity seems to progressively increase with time during 2009 (CF in Figure 2). The cluster of seismicity continues to be active into 2010.

4. Seismological Damage Zone of the L'Aquila Fault

[40] We use the aftershock distribution to estimate the width of what we have called a seismological damage zone (SDZ). The SDZ is defined as the width where 95% of the aftershocks (i.e., 4 times the standard deviation of the distribution) occurs perpendicularly to the L'Aquila fault, which we identify as the plane hosting the main shock hypocentre (large red star in Figure 7) and intersecting with the co-seismic rupture at the surface along the PaF. The resulting

plane strikes N133°E and dips 50° to the SW. We divide the fault plane in 10 rectangular boxes 2 km long along strike (boxes from 1 to 10 in Figure 7). For each box, we measure the distance orthogonal to the fault plane for each aftershock and compute the number of events occurring every 100 m within 3 km from the fault plane (0 km distance in the histograms). To better appreciate the along strike geometrical complexities of the real AF surface in relationship to the modeled planar surface indicated by the 0 km distance in the histograms, we highlight the peaks of the distribution with gray lines in each histogram. Also, in order to identify those surfaces where the largest seismic energy has been released, we report the location of the largest magnitude events and the cumulative moment magnitude (M_o) for each box (red stars and green lines in the histograms, respectively). Finally, to relate the width and the complexity of the SDZ with the main shock co-seismic slip distribution, we project onto a down-dip cross section the co-seismic slip distribution computed by *Cirella et al*. [2012] (red thick lines in Figure 7) together with the seismicity occurring within ± 0.5 km from the fault plane (red and gray dots for foreshocks and aftershocks, respectively).

[41] The peak in event distribution (gray bar in the histograms) coincides with the position of the modeled fault plane (0 km distance) only in the sector of the fault plane where the main shock and the other large magnitude earthquakes nucleated on the AF (histograms 3–7 in Figure 7). In contrast, the peak in event distribution occurs at distances as large as 1–1.5 km from the ideal fault plane near both the north-western and south-eastern fault termination (histograms 1–2 and 8–10 in Figure 7, respectively). This implies that the AF cannot be approximated with a planar surface for its entire length, but a more complex geometry is needed, to account for along strike geometrical complexities.

[42] The width of the SDZ shows strong variations along strike. It is narrower in the central portion of the fault with an average width of 300 m (histograms 3–5 in Figure 7), while it is wider at both the fault termination toward the NW and SE with average widths from 500 to 1500 m, respectively (histograms 1–2 and 7–10). Furthermore, the aftershocks show a bi-modal or tri-modal distribution at the two fault tips due to the presence of secondary structures located both in the hanging wall and footwall of the main plane (see gray arrows pointing to the off-fault secondary structures in histograms 2 and from 7 to 10). The largest width (1500 m) is observed at the southern termination of the fault plane (histograms 9 and 10 in Figure 7 corresponding to cross sections 2–5 in Figure 6). This is the direction of largest rupture directivity [*Pino and Di Luccio*, 2009] and sustained slowly decaying seismicity (SF in Figure 2).

[43] Finally, we observe an asymmetry in the distribution of the deformation with a larger number of aftershocks occurring in the hanging wall of the main shock rupture zone. This finding is consistent with field geology based studies, which observe an asymmetric distribution in the fracture density around normal faults accompanied by asymmetric damage zone widths [e.g., *Berg and Skar*, 2005]. A similar asymmetry was also observed for the Colfiorito normal faulting earthquakes [Chiaraluce et al., 2003].

[44] The aftershock distribution along the fault plane shows a strong anti-correlation with the co-seismic slip distribution (red thick lines in Figure 7).

5. Pattern of Clusters of Similar Earthquakes

[45] In order to characterize the rheological properties and the mechanical behavior of the different segments of the fault system, we investigate the presence of clusters of similar earthquakes. To identify similar earthquakes, we first compute waveform cross-correlation measurements for all earthquake pairs with hypocenter separations ≤ 5 km, over an 8 s window, including 1 s before and 7 s after the *P* wave arrival. Such a long window length allows to search for waveforms showing high similarity along the entire *P* and *S* wave and coda trains (step 7 in Figure 3). Then we search for those event pairs that produce a cross-correlation coefficient $CC \geq 0.96$ among the entire window length at five or more common stations, and we create families linking all the events that satisfy these selection criteria. With this procedure, we identify 1847 similar events belonging to 425 clusters. The number of events in each cluster ranges from 3 to 24. Each cluster is then relocated with the *hypoDD* code by using delay times from correlation data only [*Schaff and Beroza*, 2004]. Several factors indicate that the relocations are robust: (1) hypocentral location errors computed using the SVD, i.e., Singular Value Decomposition mode [*Waldhauser*, 2001], are less than 5 m; (2) many event pairs have delay time measurements at more than 40 stations and over 100 combined *P* and *S* wave readings; (3) RMS values on the order of 0.005 s; (4) relocation of clusters using *P* or *S* wave delay times alone yield very similar images. An inspection of waveforms from the largest cluster, recorded at the temporary station RM06 (Figure 8b) reveals the high degree of similarity of these nearly identical waveforms, confirming that a source effect for all 24 events is common.

[46] We display in Figure 9 examples of three similar event clusters showing a map view, a NE-striking cross section, and recurrence time intervals. The first cluster (Figure 9a) is composed of 10 events and occurred during the foreshock sequence, between 23 January and 13 February 2009. Waveforms of those events are the ones shown in Figure 8a. The magnitude ranges from 1.1 to 1.7 (histogram in Figure 9a). Looking at the cross section, we can appreciate how those events image a steeply SW-dipping plane at high-angle (section AA′) with a consistent composite focal mechanism solution. It is worth noting the scale of this fault, which is about 100 m long. This cluster nucleates at the base of the patch that ruptured the AF in the M_W 6.1 earthquake (see the arrow in section 10 in Figure 10). The largest cluster of the sequence is composed of 24 events occurring during the aftershock sequence between 17 and 22 April with $0 \leq M_L \leq 1.1$ (waveforms in Figure 8b) and is shown in Figure 9b. Again, single events image a SW-dipping plane with a coherently oriented composite focal mechanism (section AA′). This cluster nucleates at the base of the secondary fault in the transition zone between the two AF and CMPF major faults (red dot in section 12 in Figure 10). The last cluster shown in Figure 9c includes 12 earthquakes occurring between 22 May and 19 July 2009 with M_L in the 0.4 and 1.3 range. Most events have overlapping rupture areas and show a NE-dipping plane in cross section consistent with the composite focal mechanism. This cluster occurs along a minor fault zone at the southern termination of the fault system (see the arrow in section 3 in Figure 10), and it spans a time window of about 2 months (histogram in Figure 9c), which agrees with the long-lasting

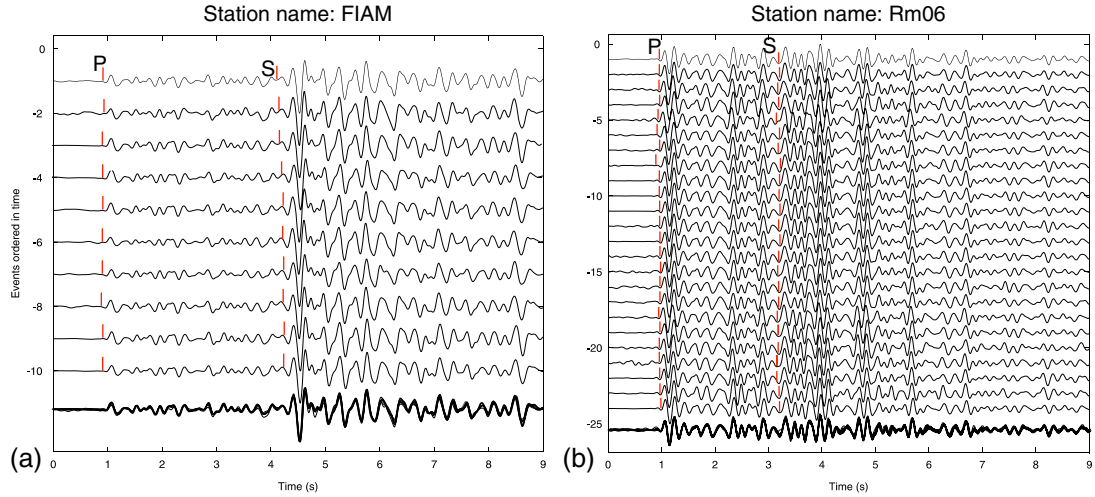

Figure 8. (a) 10 vertical component highly similar waveforms aligned on the correlated *P* wave train from an aftershock cluster recorded at the permanent station FIAM during the foreshock sequence; (b) 24 similar waveforms from an aftershock sequence cluster at the temporary station RM06. Waveforms are filtered in the 1–15 Hz range. Red ticks are automatic *P* and *S* wave onsets. Bottom traces show all waveforms superposed. Note the high similarity between all waveforms having correlation coefficient ≥ 0.96. Each trace is normalized by the maximum amplitude of the waveform.

seismic decay that characterizes the southern termination of the fault (SF in Figure 2).

[47] Magnitudes of these events are in the 0 to 1.6 range corresponding to an estimated source radius of 5 to 33 m based on circular crack model using a 3 MPa stress drop. This rupture dimension is in the range of our relative location uncertainty (see black crosses in map and cross section in Figure 9). Since not all events are located in each other's rupture areas, they appear to contribute to the breakage of a larger patch of the fault plane. We will explore possible reasons for this issue in following sections.

[48] Single clusters span both short-lived (1 week to 1 month) and long-lived (up to 2 months) time intervals (histograms in Figure 9). The recurrence intervals for the clusters shown in Figure 9 and for other clusters not shown do not always demonstrate the same behavior and range from almost a-periodic to rather periodic.

[49] To highlight the location of the 425 clusters of similar events in relation to individual faults, we plot them with respect to simplified fault planes inferred from the relocated seismicity distribution (Figure 10). We use the same color-coded scheme reported in Figure 2 to indicate the number of events in each cluster, ranging from 3 to 24. Sections in Figure 10 are numbered in the same way as in Figure 6. We highlight with an arrow the location of the three clusters described in Figure 9. We observe that the spatial distribution of the clusters in the fault system is not random but they occur on particular sectors of the single fault segments. Sequences with 3 to 5 similar events are widespread (blue and green dots in Figures 2 and 11, respectively), while sequences with at least 10 events (yellow dots) concentrate (1) at the tips (both at basal and shallow termination) of the two major faults (section 10 for the AF and sections 14 and 15 for the CMPF in Figure 10), (2) at the intersection between minor structures and the major AF and CMPF (sections 7 and 14, respectively), (3) along the flat portion of the CMPF, at the junction with the sub-vertical structure in the fault footwall (section 14 in Figure 10), and (4) on small sub-parallel faults observed both at the southern termination of the AF and in the Cittareale cluster (sections 3 and 22 in Figure 10, respectively). A point worth mentioning is the mechanical behavior observed at the lower tip of the secondary structure located in the AF footwall in the transition zone, where the 24-events cluster occurs together with three additional clusters with $\geq$10 events (cluster C and red and yellow dots in section 12 in Figure 10). Significantly, a large number of similar event clusters occur at the base of the activated major and secondary faults, coinciding with the abrupt and laterally continuous seismicity cutoff observed around 10 km depth (sections 10 to 12 in Figure 11). This finding is also apparent in the histogram in Figure 11, which shows the distributions as number of events with depth, of clusters of similar events and aftershocks (gray and black histograms, respectively). Both histograms show a clear peak at 9 km depth, confirming a major seismicity cutoff at this depth and suggesting a peculiar (i.e., creeping) mechanical behavior characterizing this horizon.

6. Discussion

6.1. Inferences on the Mechanical Properties of the Faults

[50] The mechanism of genesis of clusters of similar earthquakes is debated. *Nadeau and McEvilly* [1999] suggested that similar waveforms are produced by stuck patches in an otherwise creeping fault that repeatedly rupture the same asperity. Other proposed physical models for repeating earthquakes which include weak asperities at the border between larger locked and creeping patches on the fault plane [*Sammis and Rice*, 2001] or creeping patches that strain harden until they fail seismically [*Beeler et al.*, 2001]. In each of these proposed physical models, the presence of creeping patches adjacent to asperities plays an important role in cyclically loading patches on a fault that undergo stick-slip failure.

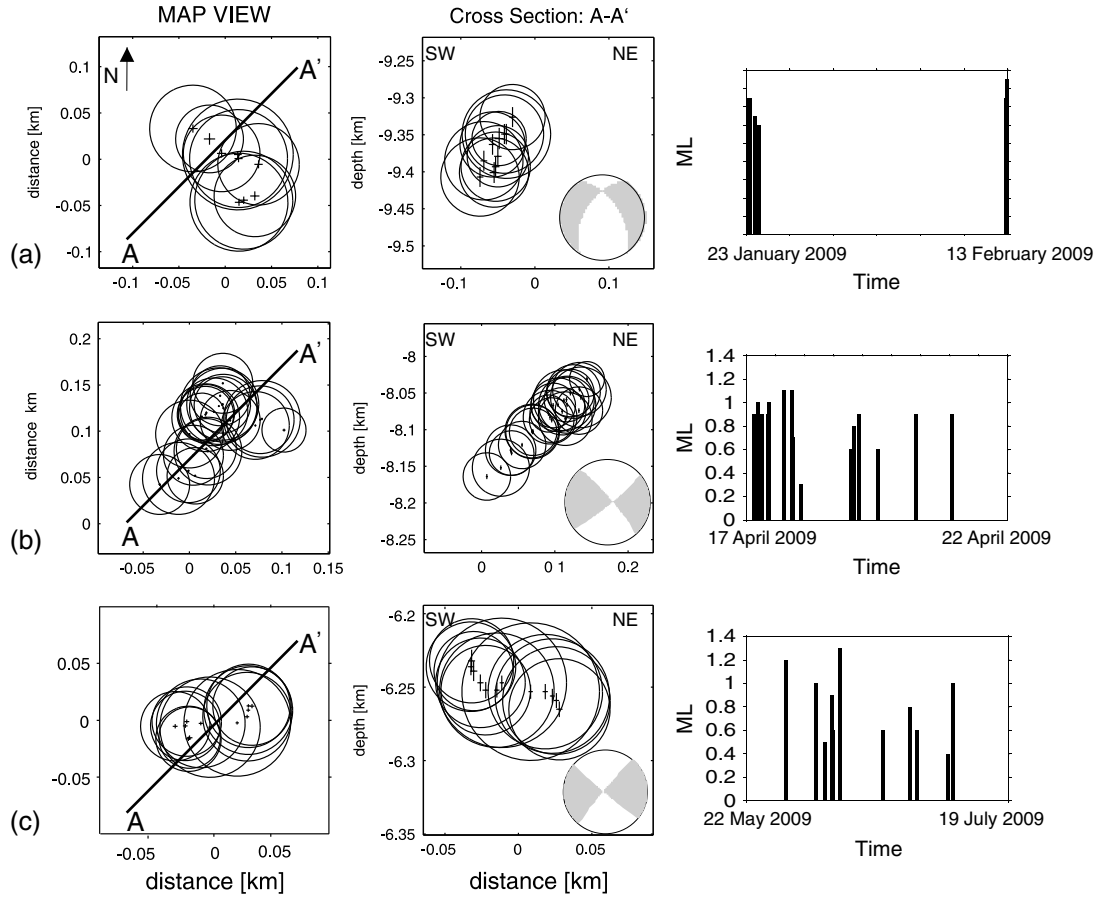

Figure 9. Plot showing map and fault perpendicular fault cross -ection view of three clusters of similar earthquakes. Circles indicate the approximate source dimension, assuming a 3 MPa circular constant stress drop source while black crosses indicate 2-sigma location errors. In cross-section view (AA′), we also show cumulative focal mechanisms for all events belonging to the cluster. Histograms report the M_L variation with time for single events in the cluster. Waveforms related to clusters 1 and 2 are shown in Figures 8a and 8b, respectively.

[51] In our dataset, similar earthquake clusters occur on portions of the fault system characterized by different geometry, lithology, depth, and mechanical properties. This suggests that different mechanisms might control the location and size of the clusters. We propose three main different interpretations for clusters nucleating on different portions of the fault system:

[52] 1. A major geometric control could explain those clusters occurring at the intersection between minor structures and the major faults (e.g., sections 1, 3, 7, and 14 in Figure 10) and those occurring at the tip of major and minor structures (e.g., sections 6, 11, and 12 in Figure 10). In both cases, geometrical complexities seem to favor stress concentration on small fault patches that can produce highly similar events with time.

[53] 2. Clusters occurring at the base of the high-angle normal faults at about 9 km depth (sections 10–12 in Figure 10 and histogram in Figure 11) are possibly suggestive of a major rheological transition at this depth where the stress concentrates between high-angle normal faults that undergo unstable sliding and a basal discontinuity which might be characterized by a mostly velocity strengthening (i.e., creeping) behavior.

[54] 3. Finally, another mechanism might be responsible for those clusters occurring at both the southern and northern terminations of the fault system (sections 3, 20, and 21 in Figure 10 and the cluster shown in Figure 9c). In both areas, regular seismicity and similar event clusters occur on small sub-parallel faults with dimensions on the order of tens of meters, possibly resembling a multilayer geometry, as suggested by *Chiaraluce* [2012]. On these structures, the seismicity production shows a long-lasting behavior together with long-lived clusters (up to 2 months; see yellow clusters in the SF and CF sectors in Figure 2). We speculate that the high sustained seismic release together with long-lived similar event clusters at the fault terminations might be suggestive of the presence of fluids within the fault volume, which could lower the effective normal stress and favor the buildup of short-lived high pore fluid pressures to facilitate aseismic creep.

6.2. The Role of Aftershocks in Fault Growth Processes

[55] The internal structure of the AF, as described by the aftershock distribution (Figure 7), is composed of two major elements: (a) an internal strand of localized deformation, which coincides with the peak of the aftershock seismicity

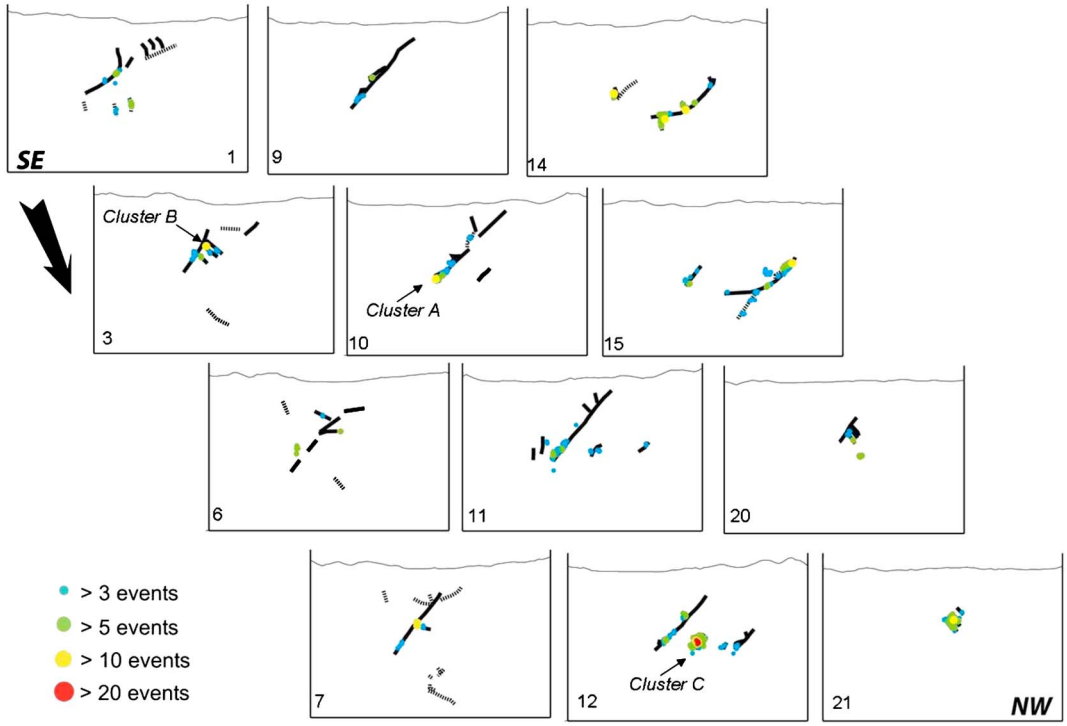

Figure 10. Vertical SW-NE oriented sections showing the location of 425 clusters of co-located events analyzed in this study together with a cartoonish representation of the major structural elements of the activated normal fault system. Sections follow the same numeration (1 to 21) used in Figure 6. Here we select the most significant sections. Clusters are color-coded to indicate the number (*N*) of events in each cluster.

distribution and of the seismic moment release and with the nucleation of the largest magnitude events (gray bars, green lines, and red stars in the histograms in Figure 7, respectively), and (b) an external zone of intense fracturing characterized by variable widths along strike and depth (i.e., the width enclosing 95% of the aftershocks distributions in Figure 7), which we have called a seismological damage zone (SDZ).

[56] The width of the SDZ shows major variations along strike: it is about 300 m thick in the portion of the fault where the main shock nucleated, but it is considerably thicker at fault tips, with the largest values (up to 1500 m) toward the SE, where the rupture directivity is reported [*Pino and Di Luccio*, 2009]. Other estimates for the damage zone width for the L'Aquila event, obtained by modeling fault zone guided waves of aftershocks, show values of 280 m ± 40 m [*Calderoni et al.*, 2010], which are comparable with our estimates.

[57] Both geophysical estimates of the SDZ show values slightly larger when compared to damage zone widths observed at the outcrop scale of normal faults developed in carbonate-bearing rocks. For example, *Micarelli et al.* [2003] estimate a damage zone of 25 to 100 m for normal faults in the Corinth Gulf (Greece), while *Agosta and Aydin* [2006] report a 100 m damage zone width for a 10 km long normal fault in Central Italy. However, while comparing geophysical and geological observations, it is important to point out that damage zone widths depend on (i) the faulting mechanism, i.e., whether reverse, normal, strike slip, or oblique; (ii) the amount of fault displacement, with thicker damage zones for larger faults [*Vermilye and Scholz*, 1998] compared to smaller/younger faults; and (iii) the different nature of the protolith. Also, the width of damage zones can vary according to the number of seismic cycles experienced by a single fault.

[58] Following these considerations, and taking into account the spatial coincidence of the peak of the aftershock distribution (gray bars), the nucleation of the largest shocks (red stars), and the cumulative seismic moment (green lines) to image a principal slipping zone bordered by a SDZ with variable width along the fault strike, we propose that the SDZ identified by aftershock distribution corresponds to the damage zone observed at the outcrop scale. This strongly supports the idea that the co-seismic rupture and the early postseismic deformation (i.e., aftershocks) can accrue the damage around faults, playing an important role in fault growth processes. This agrees with the co-seismic damage model proposed by *Rice et al*, [2005], which suggest that off-fault damage during the aftershock sequence can be triggered by the passing of a dynamic rupture pulse. Furthermore, the observed pattern of damage, with a larger SDZ at the south-eastern tip of the L'Aquila fault, where the unilateral rupture directivity has been reported [*Pino and Di Luccio*, 2009], further strengthens our observations. Accordingly, this agrees with the accepted process zone model [*Cowie and Scholz*, 1992] that predicts that damage zone width should always be largest at a propagating fault tip where displacement is lowest and where a large amount of stress is concentrated.

6.3. Seismicity Distribution During the Co-seismic and the Early Postseismic Phases

[59] Another reason to accurately characterize the internal structure of fault zones using the seismicity distribution is to

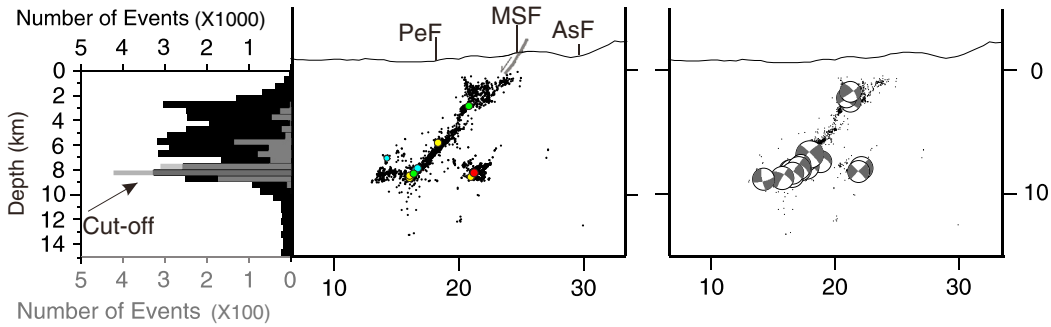

Figure 11. Section summarizing geometry, kinematics, and similar events occurrence of the L'Aquila fault. The histogram on the left compares the number of events versus depth of the "regular" seismicity (black) and of similar events clusters (gray). Note the different scale for the regular seismicity (*1000 in black) and for similar events clusters (*100 in gray). The black arrow indicates the abrupt seismicity cutoff with depth discussed in the text.

map geometrical complexities along the fault plane with the aim to investigate whether and how they can control rupture nucleation, propagation, and arrest [e.g., *Boatwright and Cocco*, 1996]. In order to explore this aspect, we have investigated the distribution of foreshocks and aftershocks and clusters of similar earthquakes occurring within ±500 m from the L'Aquila fault plane in relation to the co-seismic slip proposed by *Cirella et al*. [2012] and the postseismic (i.e., after slip) slip distribution computed for the early 180 days by *D'Agostino et al*. [2012] via modeling GPS and InSAR data (Figures 13a and 13b, respectively). Note that the co-seismic and postseismic slip models (Figures 13a and 13b) have been computed on two planes which slightly differ in strike and dip. This results in a different projection of seismic events on the fault plane, thus making the comparison of the two images not completely straightforward.

[60] In Figure 12a, we observe that very few aftershocks nucleate within the main shock co-seismic rupture areas (red thick lines), in agreement with the anti-correlation of slip and aftershocks seen elsewhere, e.g., Morgan Hill, 1984 [*Schaff et al*., 2002]; Colfiorito, 1997 [*Chiaraluce et al*., 2003]; Parkfield, 2004 [*Bakun et al*., 2005; *Johanson et al*., 2006], and consistent with the interpretation that aftershocks occur in regions where the stress level is high due to increased loading away from the area of greatest moment release [e.g., *Aki*, 1979]. In Figure 6, this behavior is envisaged by the lack of seismicity between 5 to 0 km depth in the up-dip direction of the main shock (sections 9a and 9b), in correspondence with the up-dip patch of co-seismic slip [*Cirella et al*., 2012].

[61] Focusing on the main shock nucleation volume (green inset in Figure 12a), we note that (i) foreshocks concentrate in the region at the base of the activated L'Aquila fault plane (red dots in Figure 12a) and (ii) the seismicity distribution highlights a relatively aseismic region located in between the foreshocks and the onset of the up-dip rupture propagation (highlighted by the thick gray arrow pointing up-dip in Figure 12a). *Di Stefano et al*. [2011] reported on a complex rupture onset of the M_W 6.1 main shock characterized by an initial emergent phase (EP), associated with a small seismic moment release, followed by an impulsive phase (IP) characterized by both larger moment release and high rupture speed (black and red stars in Figure 12, respectively). The authors interpreted this complex *P* wave arrival in terms of heterogeneities of material properties (i.e., V_P and V_P/V_S structure) along the fault plane between the EP and the IP. Here, we emphasize that the aseismic region coincides quite well with the region between the EP and IP phases (area identified by the green inset in Figure 12a). Interestingly, clusters of similar earthquakes occurring in the foreshock sequence surround the aseismic patch (light blue dots in Figure 12a), suggesting that loading stress was present in the nucleation volume during the foreshock sequence which may have favored the unstable dynamic rupture of the main shock [e.g., *Kato et al*., 2012], even if none of those clusters occurred in the last 7 days before the main shock. Furthermore, the absence of clusters of similar earthquakes encompassing the fore-aftershock sequence suggests that a variation in the physical properties of the nucleation region might have happened due to the main shock occurrence.

[62] Areas of postseismic slip mostly encircle the main co-seismic slip portion of the fault (Figures 12a and 12b) with a large amount of aftershocks occurring in high after-slip zones. In detail, three regions of large after slip have been reported by *D'Agostino et al*. [2012], indicated by capital letters A, B, and C in Figure 12b. We will limit our discussion to regions A and B since the patch C lies in a region of the fault where the after slip is poorly resolved [*D'Agostino et al*., 2012]. In region A, located at shallow depth on the NW corner of the AF, aftershocks directly match the surface trace of the MSF, where minor faults branching off the AF are observed (section 10 in Figure 6). Thus, we share the hypothesis formulated by some authors [e.g., *Amoruso and Crescentini*, 2009; *Wilkinson et al*., 2010; *D'Agostino et al*., 2012] that the postseismic slip on the patch A might have contributed to the development of surface fractures along the MSF segment. Also, this hypothesis agrees with field geology based data, which report a postseismic increase of opening and throw on cracks and fractures along the MSF in the weeks following the main shock [*Boncio et al*., 2010].

[63] The largest after-slip patch (up to 17 cm) is located on the SE corner of the fault between 6 and 9 km depth (B in Figure 12b), matching with a large number of aftershocks encircling the main co-seismic slip to the SE. In this region

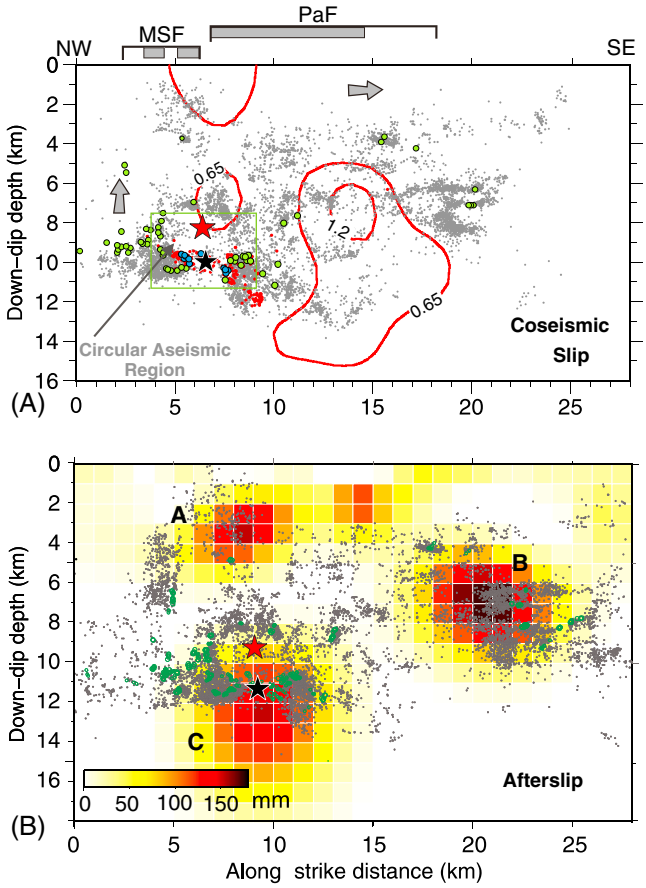

Figure 12. (a) Down-dip section (strike N133°E and dip 50° to the SW) of the L'Aquila fault plane containing EP and IP main shock hypocenter locations (black and red stars, respectively), foreshocks and aftershocks located within ±500 m from the fault plane (red and gray dots, respectively), similar events clusters in the foreshock and aftershock sequence (light blue and green dots, respectively), the co-seismic slip (red solid contours) from *Cirella et al.* [2012], and Mt. Stabiata (MSF) and Paganica (PaF) mapped faults (thick black lines) and surface ruptures (thick gray lines) [*Boncio et al.* 2010]; the thick gray arrows indicate the temporal evolution of the rupture; the green inset indicates the main shock's nucleation volume. (b) Cumulative after-slip distribution on the fault plane (strike N140°E and dip 47° to SW), computed by inverting GPS and InSAR data between 12 April and the following 180 days [*D'Agostino et al.*, 2012]. The capital letters A, B, and C indicate after-slip features discussed in the text. The EP and IP main shock hypocenter (black and red stars, respectively) plus aftershocks occurring within ±500 m from the fault plane and similar events are also reported (gray and green dots, respectively). Note the different geometry of the two fault planes used to compute the co-seismic and postseismic slip distribution.

of the fault system, the geometry of the fault shows a strong increase in geometrical complexity with aftershocks occurring on small sub-parallel fault strands instead of being concentrated on the major AF plane (sections 2–5 in Figure 6). The sharp transition of co-seismic slip and after slip, plus the evidence of dispersed aftershocks on this portion of the fault, suggests that geometrical complexities might have arrested the propagation of co-seismic rupture and triggered significant after slip and aftershocks. This agrees with the observed seismicity pattern characterized by a very low decay rate when compared to the other sectors of the fault system (SF in Figure 2).

6.4. Inferences on the Seismotectonic Setting

[64] A remarkable feature of the entire fault system is the abrupt seismicity cutoff around 9 km depth (Figures 7 and 12). In the Campotosto region, the cutoff is formed by a nearly horizontal active basal discontinuity imaging a listric geometry. Below the L'Aquila fault segment (Figure 11), this feature is less outstanding, but the seismicity does image a nearly horizontal discontinuity at the base of the high-angle fault (sections 10–12 in Figure 6), with coherent focal mechanisms. There are different possible interpretations for this discontinuity. It could represent a major lithological change, but its regional continuity through different lithological formations seems to exclude this hypothesis [*Chiaraluce et al.*, 2011a]. It could point to the brittle-ductile transition [*Scholz*, 2002], but some events of different magnitude do occur at larger depths both in the L'Aquila (i.e., the M_W 5.4 aftershock which nucleated at ~15 km of depth; section 5 in Figure 6) and in the Campotosto area (events occurring in the CMPF footwall; sections 14 and 15 in Figure 6). Lastly, this structural element might correspond to the flat portion of a thrust inherited from the previous Mio-Pliocene compressional tectonic phase, which has been reactivated (i.e., inverted) under the Pleistocene-Present extensional environment (i.e., a basal detachment). Unfortunately, in this area, there are no deep seismic profiles to test this hypothesis.

[65] The spatiotemporal distribution of similar event clusters can help to shed light on the mechanical behavior of this basal discontinuity. A large number of similar events nucleate at the seismicity cutoff depths as illustrated by the histogram of Figure 11. These events nucleate at the juncture between high-angle SW-dipping normal faults and the low-angle (<20°) discontinuity (sections 10, 12, and 14 in Figures 10 and 11). This is suggestive of a major rheological/mechanical transition occurring at this depth where the stress concentrates between high-angle normal faults that undergo unstable sliding (i.e., stick slip) and a basal low-angle discontinuity characterized by a mostly velocity strengthening (i.e., creeping) behavior (see Figure 13 for a schematic representation). We speculate that this feature characterizing this portion of the Central Apennines might describe how normal faults in general terminate at depth. Also, it might suggest a seismotectonic style in which the creeping basal detachment can accrue the stress concentration at the base of high-angle normal faults, triggering future earthquakes (Figure 13).

7. Conclusions

[66] In this paper, we have produced and analyzed a comprehensive normal faulting aftershock catalog made up of more than 60K precisely located earthquakes spanning 1 year, including 4 months of foreshocks. The dataset has a magnitude of completeness more than 1 unit lower than other state-of-the-art earthquake catalogues for similar tectonic environments.

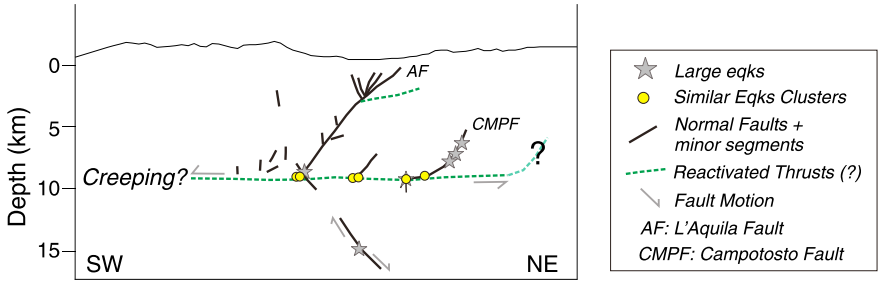

Figure 13. Cartoon showing the proposed seismotectonic model of the area.

[67] The intrinsic precision and accuracy of this dataset makes it an important tool for statistical seismology studies. Since the detailed sampling of the spatiotemporal evolution of the seismic sequence has a strong control on the redistribution of elastic stresses and on the triggering of subsequent earthquakes [e.g., *Marsan*, 2005; *Felzer and Brodsky*, 2005], this catalogue has the potential to substantially improve methods of short-term forecast analysis [e.g., *Marzocchi and Lombardi*, 2009].

[68] The fault architecture is imaged with a resolution at the tens of meter scale and resembles the complexity observed on outcrop faults by field geologists. We have described the internal structure of the L'Aquila fault by identifying a zone of localized deformation where the largest events nucleate. This is surrounded by a region of intense fracturing characterized by variable widths along strike and depth defining a seismological damage zone (SDZ). The SDZ identified by the aftershock distribution shows geometrical patterns comparable to damage zones observed at the outcrop scale. This signifies that the co-seismic rupture and the early postseismic period (i.e., aftershocks) can accrue the damage around faults, which can play an important role in fault growth processes. Moreover, the observed geometrical complexities and heterogeneities of the fault zone seem to control rupture nucleation, propagation and arrest of the seismic slip, and its behavior during the aftershock sequence and subsequent stress recovery.

[69] The combined use of a high-resolution seismic catalogue and information on clusters of similar earthquakes helped in deciphering important aspects of the mechanical behavior of major and minor faults. In particular, the strong and laterally continuous seismicity cutoff around 9 km depth coincides with the location of a large number of similar earthquakes. This suggests that at this depth, a major rheological transition occurs where the stress concentrates between high-angle normal faults that undergo unstable sliding (i.e., stick slip) and a basal low-angle discontinuity characterized by a mostly velocity strengthening (i.e., creeping) behavior.

[70] Besides the important implications for the seismotectonic style of this portion of the Apennines, the existence of a creeping basal detachment loading the high-angle normal faults may help in better assessing the seismic hazard of single faults. Towards this goal, identifying which areas of the fault (or which single fault) are locked and accumulating elastic strain to be released during a future earthquake and which areas are slowly releasing strain through aseismic creep are essential when examining the nucleation processes and evaluating the seismic hazard. Additionally, since surface geodetic measurements can have difficulty resolving the slip in the middle to lower seismogenic zone, a correct evaluation of the strain rate could benefit from long-term studies on clusters of similar earthquakes that can furnish information down to the bottom of the seismogenic zone.

[71] **Acknowledgments.** We thank N. Seeber, B. Carpenter, A. Cirella, A. M. Lombardi, and T. Mitchell for useful discussions and F. Aldersons for the help with the MannekenPix automatic picking algorithm. We acknowledge S. Cox and D. Cowan for constructive and helpful reviews. We thank all the people at the INGV and the LGIT of Grenoble who participated in the field work and the group of Analisi Dati Sismologici at the INGV for the data archiving. L. V. is grateful to D. Melini for the patient support in the use of the INGV computer cluster (HPC facilities). L. V. was supported by the ERC St. G. Nr. 259256 GLASS project.

References

Agosta, F., and A. Aydin (2006), Architecture and deformation mechanism of a basin-bounding normal fault in Mesozoic platform carbonates, Central Italy, *J. Struc. Geol.*, *28*, 1445–1467.

Aki, K. (1979), Characterization of barriers on an earthquake fault, *J. Geophys. Res.*, *84*, 6140–6148.

Aldersons, F., R. Di Stefano, L. Chiaraluce, D. Piccinini, and L. Valoroso (2009), Automatic detection, and P and S wave picking algorithm: An application to the 2009 L'Aquila (central Italy) earthquake sequence, *Eos Trans. AGU*, *90*(52), Fall Meet. Suppl., Abstract U23B-0045.

Amoruso, A., and L. Crescentini (2009), Slow diffusive fault slip propagation following the 6 April 2009 L'Aquila earthquake, Italy, *Geophys. Res. Lett.*, *36*, L24306, doi:10.1029/2009GL041503.

Bakun, W. H., et al. (2005), Implications for prediction and hazard assessment from the 2004 Parkfield, California, earthquake, *Nature*, *437*, 969–974.

Beeler, N. M., S. H. Hickman, and T.-F. Wong (2001), Earthquake stress drop and laboratory-inferred interseismic strength recovery, *J. Geophys. Res.*, *106* (B12), doi:10.1029/2000JB900242.

Berg, S. S. and T. Skar (2005), Controls on damage zone asymmetry of a normal fault zone: Outcrop analyses of a segment of the Moab fault, SE Utah, *J. Struct. Geol.*, (27), 1803–1822, doi:10.1016/j.jsg.2005.04.012.

Boatwright, J. and M. Cocco (1996), Frictional constraints on crustal faulting, *J. Geophys. Res. 101*(B6): doi: 10.1029/96JB00405.

Boncio, P., A. Pizzi, F. Brozzetti, G. Pomposo, G. Lavecchia, D. Di Naccio, and F. Ferrarini (2010), Coseismic ground deformation of the 6 April 2009 L'Aquila earthquake (central Italy, M_W 6.3), *Geophys. Res. Lett.*, *37*, L06308, doi:10.1029/2010GL042807.

Calderoni, G., A. Rovelli, and R. Di Giovambattista (2010), Large amplitude variations recorded by an on-fault seismological station during the L'Aquila earthquakes: Evidence for a complex fault-induced site effect, *Geophys. Res. Lett.*, *37*, L24305, doi:10.1029/2010GL045697.

Chen, K. H., R. Burgmann, R. M. Nadeau, T. Chen, and N. Lapusta (2010), Postseismic variations in seismic moment and recurrence interval of repeating earthquakes, *Earth Planet. Sci. Lett.*, *299*, doi:10.1016/j.epsl.2010.08.027.

Chiarabba, C., et al. (2009), The 2009 L'Aquila (central Italy) M_W 6.3 earthquake: Main shock and aftershocks, *Geophys. Res. Lett.*, *36*, L18308, doi:10.1029/2009GL039627.

Chiaraluce, L. (2012), Unravelling the complexity of Apenninic extensional fault systems: A review of the 2009 L'Aquila earthquake (Central Apennines, Italy), *J. Struct. Geol.*, *42*, 2–18, doi:10.1016/j.jsg.2012.06.007.

Chiaraluce, L., W. L. Ellsworth, C. Chiarabba, and M. Cocco (2003), Imaging the complexity of an active normal fault system: The 1997 Colfiorito (central Italy) case study, *J. Geophys. Res.*, *108*(B6), 2294, doi:10.1029/2002JB002166.

Chiaraluce, L., L. Valoroso, M. Anselmi, S. Bagh, and C. Chiarabba (2009), A decade of passive seismic monitoring experiments with local networks in four Italian regions, *Tectonophysics*, *476*, 85–98, doi:10.1016/j.tecto.2009.02.013.

Chiaraluce, L., L. Valoroso, D. Piccinini, R. Di Stefano, and P. De Gori (2011a), The anatomy of the 2009 L'Aquila normal fault system (central Italy) imaged by high resolution foreshock and aftershock locations, *J. Geophys. Res.*, *116*, B12311, doi:10.1029/2011JB008352.

Chiaraluce, L., C. Chiarabba, P. De Gori, R. Di Stefano, L. Improta, D. Piccinini, A. Schlagenhauf, P. Traversa, L. Valoroso, and C. Voisin (2011b). The 2009 L'Aquila (central Italy) seismic sequence, *Boll. Geofis. Teor. Appl.*, *52*(3), 367–387, doi:10.4430/bgta0019.

Cirella, A., A. Piatanesi, E. Tinti, M. Chini and M. Cocco (2012), Complexity of the rupture process during the 2009 L'Aquila, Italy, earthquake, *Geophys. J. Int.*, *190*, 607–621, doi:10.1111/j.1365-246X.2012.05505.x.

Collettini C., M. R. Barchi, L. Chiaraluce, F. Mirabella, and S. Pucci (2003), The Gubbio fault: Can different methods give pictures of the same object?, *J. Geody.*, (36), 51–66, ISSN: 0264–3707

Cowie, P. A., and C. H. Scholz (1992), Growth of faults by accumulation of seismic slip, *J. Geophys. Res.*, *97*, doi:10.1029/92JB00586.

D'Agostino, N., A. Avallone, D. Cheloni, E. D'Anastasio, S. Mantenuto, and G. Selvaggi (2008), Active tectonics of the Adriatic region from GPS and earthquake slip vectors, *J. Geophys. Res.*, *113*, B12413, doi:10.1029/2008JB005860.

D'Agostino, N., D. Cheloni, G. Fornaro, R. Giuliani, and D. Reale (2012), Space-time distribution of afterslip following the 2009 L'Aquila earthquake, *J. Geophys. Res.*, *117*, B02402, doi:10.1029/2011JB008523.

D'Agostino, N., R. Giuliani, M. Mattone, and L. Bonci (2001), Active crustal extension in the central Apennines (Italy) inferred from GPS measurements in the interval 1994–1999, *Geophys. Res. Lett.*, *28*, 2121–2124, doi:10.1029/2000GL012462.

De Paola N., C. Collettini, D. R. Faulkner and F. Trippetta (2008), Fault zone architecture and deformation processes within evaporitic rocks in the upper crust, *Tectonics*, *27*, ISSN: 0278–7407, doi: 10.1029/2007TC002230.

Di Luccio, F., G. Ventura, R. Di Giovambattista, A. Piscini, and F. R. Cinti (2010), Normal faults and thrusts reactivated by deep fluids: The 6 April 2009 M_W 6.3 L'Aquila earthquake, central Italy, *J. Geophys. Res.*, *115*, B06315, doi:10.1029/2009JB007190.

Di Stefano, R., F. Aldersons, E. Kissling, P. Baccheschi, C. Chiarabba, and D. Giardini (2006), Automatic seismic phase picking and consistent observation error assessment: Application to the Italian seismicity, *Geophys. J. Int.*, *165*, 121–134.

Di Stefano, R., C. Chiarabba, L. Chiaraluce, M. Cocco, P. De Gori, D. Piccinini, and L. Valoroso (2011), Fault zone properties affecting the rupture evolution of the 2009 (M_W 6.1) L'Aquila earthquake (central Italy): Insights from seismic tomography, *Geophys. Res. Lett.*, *38*, L10310, doi:10.1029/2011GL047365.

Diehl, T., N. Deichmann, E. Kissling, and E. Husen (2009), Automatic S-wave picker for local earthquake tomography, *Bull. Seism. Soc. Am.*, *99*, 3, 1906–1920, doi: 10.1785/0120080019.

EMERGEO Working Group (2009), Evidence for surface rupture associated with the M_W 6.3 L'Aquila earthquake sequence of April 2009 (central Italy), *Terra Nova*, *22*, 43–51, doi:10.1111/j.1365-3121.2009.00915.x.

Felzer, K. R., and E. E. Brodsky (2005), Testing the stress shadow hypothesis, *J. Geophys. Res.*, *110*, B05S09, doi:10.1029/2004JB003277.

Fréchet, J. (1985), Sismogenése et doublets sismiques, thése d'Etat, 206 pp., Univ. é Sci. et Méd. de Grenoble, Grenoble, France.

Galadini, F., and P. Galli (2000), Active tectonics in the central Apennines (Italy)—Input data for seismic hazard assessment, *Nat. Hazards*, *22*, 225–268, doi:10.1023/A:1008149531980.

Galli, P., B. Giaccio, and P. Messina (2010), The 2009 central Italy earthquake seen through 0.5 Myr-long tectonic history of the L'Aquila faults system, *Quat. Sci. Rev.*, *29*, 3768–3789.

Galli, P., B. Giaccio, P. Messina, E. Peronace and G. M. Zuppi (2011), Palaeoseismology of the L'Aquila faults (central Italy, 2009, M_W 6.3 earthquake): Implications for active fault linkage, *Geophys. J. Int.*, *187*, 1119–1134, doi: 10.1111/j.1365-246X.2011.05233.x.

Geller, R. J., and C. S. Mueller (1980), Four similar earthquakes in central California, *Geophys. Res. Lett.*, *7*, 821–824, doi:10.1029/GL007i010p00821.

Herrmann, R. B., L. Malagnini, and I. Munafò (2011), Regional moment tensors of the 2009 L'Aquila earthquake sequence, *Bull. Seismol. Soc. Am.*, *101*, 975–993, doi:10.1785/0120100184.

Hunstad, I., G. Selvaggi, N. D'Agostino, P. England, P. Clarke, and M. Pierozzi (2003), Geodetic strain in peninsular Italy between 1875 and 2001, *Geophys. Res. Lett.*, *30*(4), 1181, doi:10.1029/2002GL016447.

Johanson, I. A., E. J. Fielding, R. Rolandone and R. Bürgmann (2006), Coseismic and postseismic slip of the 2004 Parkfield earthquake from space-geodetic data, *Bull. Seism. Soc. Am.*, *96*, S269–S282.

Kato A., K. Obara, T. Igarashi, H. Tsuruoka, S. Nakagawa, and N. Hirata (2012), Propagation of slow slip leading up to the 2011 M_W 9.0 Tohoku-Oki earthquake, *Science*, *335*, 705, DOI:10.1126/science.1215141

Lahr, J. C. (1989), HYPOELLIPSE/version 2.00: A computer program for determining local earthquakes hypocentral parameters, magnitude and first motion pattern, *U.S. Geol. Surv., Open File Rep.*, *89–116*, 162.

Lucente, F. P., P. De Gori, L. Margheriti, D. Piccinini, M. Di Bona, C. Chiarabba, and N. P. Agostinetti (2010), Temporal variation of seismic velocity and anisotropy before the 2009 M_W 6.3 L'Aquila earthquake, Italy, *Geology*, *38*, 1015–1018, doi:10.1130/G31463.1.

Malagnini, L., F. P. Lucente, P. De Gori, A. Akinci, and I. Munafo' (2012), Control of pore fluid pressure diffusion on fault failure mode: Insights from the 2009 L'Aquila seismic sequence, *J. Geophys. Res.*, *117*, B05302, doi:10.1029/2011JB008911.

Malinverno, A., W. B. F. Ryan (1986), Extension in the Tyrrhenian Sea and shortening in the Apennines as result of arc migration driven by sinking of the lithosphere, *Tectonics*, *5*, 227–245.

Margheriti, L., et al. (2011), Rapid response seismic networks in Europe: Lessons learnt from the L'Aquila earthquake emergency, *Ann. Of Geoph. 54*, 4, 2011; doi: 10.4401/ag-4953.

Marone, C., J. E. Vidale, and W. Ellsworth (1995), Fault healing inferred from time dependent variations in source properties of repeating earthquake, *Geophys. Res. Lett.*, *22*, 3095–3098.

Marsan, D. (2005), The role of small earthquakes in redistributing crustal elastic stress, *Geophys. J. Int.*, *163*, 141–151, doi:10.1111/j.1365-246X.2005.02700.x

Marzocchi, W., and A. M. Lombardi (2009), Real-time forecasting following a damaging earthquake, *Geophys. Res. Lett.*, *36*, L21302, doi:10.1029/2009GL040233.

Micarelli, L., I. Moretti, and J. M. Daniel (2003), Structural properties of rift-related normal faults: The case study of the Gulf of Corinth, Greece, *J. Geodyn.*, *36*(1–2), 275–303, doi:10.1016/S0264-3707(03)00051-6.

Mitchell T. and D. R. Faulkner (2009). The nature and origin of off-fault damage surrounding strike-slip fault zones with a wide range of displacements: A field study from the Atacama fault system, northern Chile. *J. Struct. Geol.*, *31*, 802–816, doi:10.1016/j.jsg.2009.05.002.

Montone, P., M. T. Mariucci, S. Pondrelli, and A. Amato (2004), An improved stress map for Italy and surrounding regions (central Mediterranean), *J. Geophys. Res.*, *109*, B10410, doi:10.1029/2003JB002703.

Nadeau, R. M. and T. V. McEvilly (1999), Fault slip rates at depth from recurrence intervals of repeating microearthquakes, *Science*, *285*, 718–721.

Paige, C. C., and M. A. Saunders (1982), LSQR: An algorithm for sparse linear equations and sparse least squares, *ACM Trans. Math. Softw.*, *8*, 43–71.

Parotto, M., and A. Praturlon (1975), Geological summary of the central Apennines, in Structural Model of Italy, *Quad. Ric. Sci.*, 90, 257–311, Cons. Naz. delle Ric., Rome.

Patacca, E., P. Scandone, E. Di Luzio, G. P. Cavinato, and M. Parotto (2008), Structural architecture of the central Apennines: Interpretation of the CROP 11 seismic profile from the Adriatic coast to the orographic divide, *Tectonics*, *27*, TC3006, doi:10.1029/2005TC001917.

Peng, Z., J. E. Vidale, C. Marone, and A. Rubin (2005), Systematic variations in recurrence interval and moment of repeating aftershocks, *Geophys. Res. Lett.*, *32*, L15301, doi:10.1029/2005GL022626.

Pino, N. A., and F. Di Luccio (2009), Source complexity of the 6 April 2009 L'Aquila (central Italy) earthquake and its strongest aftershock revealed by elementary seismological analysis, *Geophys. Res. Lett.*, *36*, L23305, doi:10.1029/2009GL041331.

Pondrelli, S., S. Salimbeni, A. Morelli, G. Ekstrom, M. Olivieri, and E. Boschi (2010), Seismic moment tensors of the April 2009, L'Aquila (Central Italy), earthquake sequence, *Geophys. J. Int.* (2010) *180*, 238–242 doi: 10.1111/j.1365-246X.2009.04418.x

Poupinet, G., W. L. Ellsworth, and J. Frechet (1984), Monitoring velocity variations in the crust using earthquake doublets: An application to the Calaveras Fault, California, *J. Geophys. Res.*, *89*, 5719–5731, doi:10.1029/JB089iB07p05719.

Rice, J. R., C. Sammis, and R. Parsons (2005), Off-fault secondary failure induced by a dynamic slip pulse, *Bull. Seismol. Soc. Am.*, *95*(1), 109–134, doi:10.1785/0120030166.

Rowe, C. A., R. C. Aster, B. Borchers, and C. J. Young (2002), An automatic, adaptive algorithm for refining phase picks in large seismic data sets, *Bull. seism. Soc. Am.*, *92*(5), 1660–1674.

Sammis, C. G., and J. R. Rice (2001), Repeating earthquakes as low-stressdrop events at a border between locked and creeping fault patches, *Bull. Seismol. Soc. Am.*, *91*, 532–537.

Savage, H. M., and E. E. Brodsky (2011), Collateral damage: Evolution with displacement of fracture distribution and secondary fault strands in fault damage zones, *J. Geophys. Res.*, *116*, B03405, doi:10.1029/2010JB007665.

Schaff, D. P., and G. C. Beroza (2004), Coseismic and postseismic velocity changes measured by repeating earthquakes, *J. Geophys. Res.*, *109*, B10302, doi:10.1029/2004JB003011.

Schaff, D. P., and F. Waldhauser (2005). Waveform cross-correlation-based differential travel-time measurements at the Northern California Seismic Network, *Bull. Seismol. Soc. Am. 95*, 2446–2461, doi 10.1785/0120040221.

Schaff, D. P., G. H. R. Bokelmann, G. C. Beroza, F. Waldhauser, and W. L. Ellsworth (2002), High resolution image of Calaveras Fault seismicity, *J. Geophys. Res.*, *107*(B9), 2186, doi:10.1029/2001JB000633.

Schaff, D. P., G. Bokelmann, W. L. Ellsworth, E. Zanzerkia, F. Waldhauser, and G. C. Beroza (2004), Optimizing correlation techniques for improved earthquake location, *Bull. Seismol. Soc. Am.*, *94*, 705–721, doi:10.1785/0120020238.

Scholz, C. H. (2002), The Mechanics of Earthquakes and Faulting, Cambridge Univ. Press, Cambridge, U. K.

Schorlemmer, D., F. Mele, and W. Marzocchi (2010), A completeness analysis of the National Seismic Network of Italy, *J. Geophys. Res.*, *115*, B04308, doi:10.1029/2008JB006097.

Scognamiglio, L., E. Tinti, A. Michelini, D. S. Dreger, A. Cirella, M. Cocco, S. Mazza, and A. Piatanesi (2010), Fast determination of moment tensors and rupture history: What has been learned from the 6 April 2009 L'Aquila earthquake sequence, *Seismol. Res. Lett.*, *81*, 892–906, doi:10.1785/gssrl.81.6.892.

Uchida, N., J. Nakajima, A. Hasegawa, and T. Matsuzawa (2009), What controls interplate coupling?: Evidence for abrupt change in coupling across a border between two overlying plates in the NE Japan subduction zone, *Earth Planet. Sci. Lett.*, *283*, 111–121.

Valoroso, L., L. Improta, L. Chiaraluce, R. Di Stefano, L. Ferranti, A. Govoni, and C. Chiarabba (2009), Active faults and induced seismicity in the Val d'Agri region (southern Apennines, Italy), *Geophys. J. Int.*, *178*, 488–502, doi:10.1111/j.1365-246X.2009.04166.x.

Vermilye, J. M., and C. H. Scholz (1998), The process zone: A microstructural view of fault growth, *J. Geophys. Res.*, *103*(B6), 12,223–12,237, doi:10.1029/98JB00957.

Vidale, J. E., W. L. Ellsworth, A. Cole, and C. Marone (1994), Variations in rupture process with recurrence interval in a repeated small earthquake, *Nature*, *368*, 624–626.

Waldhauser, F. (2001), hypoDD: A program to compute double-difference hypocenter locations, U.S. Geol. Surv. Open File Rep., 01–113.

Waldhauser, F. (2009), Near-real-time double-difference event location using long-term seismic archives, with application to Northern California, *Bull. Seism. Soc. Am.*, *99*, 5, 2736–2748, doi: 10.1785/0120080294

Waldhauser, F., and W. L. Ellsworth (2000), A double-difference earthquake location algorithm: Method and application to the northern Hayward Fault, California, *Bull. Seismol. Soc. Am.*, *90*, 1353–1368, doi:10.1785/0120000006.

Waldhauser, F., and D. P. Schaff (2008), Large-scale relocation of two decades of Northern California seismicity using cross-correlation and double-difference methods, *J. Geophys. Res.*, *113*, B08311, doi:10.1029/2007JB005479.

Wiemer, S. (2001), A software package to analyze seismicity: ZMAP, *Seismol. Res. Lett. 72*, 2.

Wiemer, S., and M. Wyss (2000), Minimum magnitude of complete reporting in earthquake catalogs: Examples from Alaska, the Western United States, and Japan, *Bull. Seismol. Soc. Am.*, *90*, 859–869.

Wilkinson, M., et al. (2010), Partitioned postseismic deformation associated with the 2009 M_W 6.3 L'Aquila earthquake surface rupture measured using a terrestrial laser scanner, *Geophys. Res. Lett.*, *37*, L10309, doi:10.1029/2010GL043099.